

Section 2

Data sets, diagnostic and dynamical investigations, statistical post-processing , multi-year reanalyses and associated studies

RECONSTRUCTION OF SHORT-TERM PRECIPITATION TOTALS WITH ALLOWANCE FOR WEATHER PHENOMENA DATA

Yuri V. Alferov,
Hydrometeorological Research Center of the Russian Federation,
11-13, Bolshoi Predtechenskii per., 123242, Moscow, Russia,
e-mail: alferov@mecom.ru.

Measured precipitation totals are needed to verify developing numerical methods for precipitation analysis and prediction. However, precipitation totals measured at weather stations are frequently not consistent with standard times and accumulation periods, which makes the standardization of measured precipitation totals an important problem [1]. A method for obtaining short-term precipitation totals from longer-term ones in conjunction with other precipitation data received from weather stations is suggested.

The method is based on data from SYNOP messages (code form FM 12-IX SYNOP). We consider precipitation totals (RRR , R_{24} R_{24} R_{24}), time periods for the totals (t_R), past weather (W_1W_2 or $W_{a1}W_{a2}$), present weather (ww or $w_a w_a$), types of low and medium level clouds (C_L , C_M), fraction of the celestial dome covered by C_L or C_M (N_h), and indices of $RRRt_R$ and wwW_1W_2 groups presence (i_R , i_x).

For each message we can set a problem as follows [2]:

$$\left\{ \begin{array}{l} \left(\sum_{j=d,p,h} l_j r_j t_j - R(1-q) \right)^2 \rightarrow \min \\ 1 - t_j \geq 0, \quad j = d, p, h \\ t_j - \frac{1}{60} \geq 0, \quad j = d, p, h \\ k - \sum_{j=d,p,h} l_j t_j \geq 0 \\ r_j - a_j^{\min} \geq 0, \quad a_j^{\max} - r_j \geq 0, \quad j = d, p, h \\ q \geq 0, \quad 1 - q > 0 \\ m(r_d + r_p + r_h) - Rq \geq 0 \end{array} \right.$$

where indices mean the type of precipitation (d – drizzle, p – steady precipitation, h – heavy precipitation); R is the precipitation total for some time period T ; l_j are the hours with precipitation of type j ; r_j is the rate of precipitation of type j ; t_j is the duration of precipitation of type j (a fraction of an hour), which is assumed to be the same for any hour with precipitation of type j ; k is the number of hours with precipitation in the period T ; m is the number of hours in the period T for which there is no information about precipitation; q is the fraction of R for m hours, and a_j^{\min} and a_j^{\max} are the thresholds for the rates of precipitation of type j .

We solve the problem by the method of gradient descending with penalty functions. We use climatic values of the rate and duration of precipitation of each type as a start point for descending.

Messages from stations placed in Germany were used for verification of the method. Precipitation and weather data are sent every 3 hours from these stations. Messages may contain 3-, 6-, and 24-hour precipitation totals. Based on the method suggested, 3- and 6-hour precipitation totals were estimated from the 24-hour ones for different seasons. The results were compared to observations. The RMSE obtained for the reconstructed 3-h precipitation totals, averaged for more than 120 stations, was from 0.5 to 1.9 mm for different seasons; the correlation coefficient (CORR) was about 0.5, and the Hanssen-Kuipers discriminant with zero threshold (HKD) was approximately equal to 0.7. For the 6-h precipitation totals, RMSE was from 1.2 to 2.5 mm, CORR was about 0.6, and HKD was approximately the same as for the 3-hour totals.

We are to use satellite data as an additional condition in the problem formulation and hope that this will improve precipitation estimates.

The study was supported by the Russian Foundation for Basic Research (projects nos. 04-05-64530-a and 05-05-64575-a).

References:

1. Assimilation of clouds and precipitation, *ECMWF/EuroTRMM Workshop Proc.*, 6-9 Nov. 2000. — ECMWF, Reading, United Kingdom, 2001, 414 p.
2. Alferov, Yu.V., 2004: Estimation of precipitation for short periods using data on weather events. *Russian Meteorology and Hydrology*, no. 10.

Paradox of SST and lower tropospheric temperature trends over the tropical Pacific Ocean

Xuezhi Bai ^{1,2}, S. Cocks ², T.E. LaRow ², James J. O'Brien ² and D. W. Shin ²

1. Institute of Oceanology, Chinese Academy of Sciences

2. Center for Ocean-Atmospheric Prediction Studies, Florida State University

(xzhbai@ms.qdio.ac.cn)

Observed and modeled data were used to study the long term climate changes over the tropical Pacific Ocean, focusing on the different trends between SST and the low-mid tropospheric temperature revealed by recent satellite observations. The study indicated that various kinds of datasets confirmed the existence of differential temperature trends between the ocean surface and bulk troposphere above in terms of spatially averaged time series. The tropical Pacific SST has been warming at a rate of about 0.08 K/Dec in last 25 years, while the low-mid troposphere over the tropical Pacific has been warming at a smaller rate of about 0.04 K/Dec from MSU2LT V5.2 (MSU channel 2, low-mid tropospheric temperature) or even cooling from MSU2LT V5.1, NCEP/NCAR reanalysis 2 and ERA40 (Fig. 1a and Table 1).

Linear trend map in the tropical Pacific SSTs shows that, in past 25 years, the western Pacific has been warming while the central eastern part is cooling. A similar pattern was also found in the trend of MSU2LT V5.2, though it is more zonally symmetric than the trend in SST. Low-mid troposphere over the western Pacific has been warming at a larger rate than over the eastern Pacific. Whereas, in the old version of MSU2LT (V5.1) and NCEP2, low-mid troposphere over the eastern Pacific has been cooling since 1979 (Fig. 2). The warming in the western Pacific contributes more to this discrepancy. The enhanced zonal gradient of SSTs

induces an enhanced Walker circulation like flow in lower troposphere (Fig.3). Another mechanism involved is the land-ocean distribution. With small heat capacities, land surfaces equilibrate much more rapidly with the temperature of the overlying air mass than does the ocean, i.e., the air over land warms quicker than that over ocean. This zonal different warming rate will induce large-scale convergence circulation, driving cold air from upper level to make the lower troposphere cool over the ocean (Fig.3).

All climate models employed in this study fail to reproduce the different trends shown in the observation (Fig.1b and Table 2). AGCM forced by prescribed SST (AMIP2 simulations) predicted a warming trend in low-mid troposphere almost at the same rate as SSTs. With including all observed natural and anthropogenic forcings, coupled models (20th century climate change simulations) predicted larger warming trend in low-mid troposphere than that in SSTs (Table 3). Comparison of standard deviations of MSU2LT and equivalent MSU2LT (MSUE) computed from the AMIP2 simulations reveals that the atmosphere model could not reproduce the true response of low-mid troposphere to the SSTA in the cold tongue region (Fig. 4).

COAPS receives its base support from the Applied Research Center, funded by NOAA Office of Global Programs awarded to Dr. James J. O'Brien.

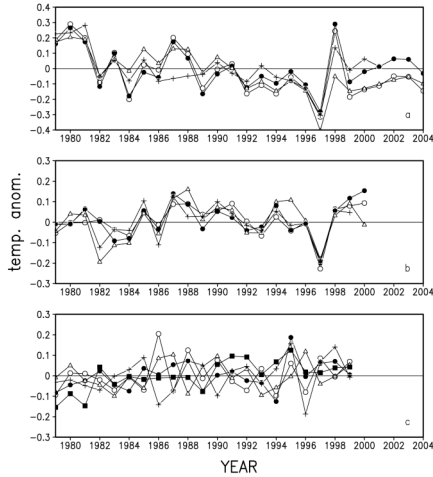


Fig.1 Annual differences of anomalies of various tropical Pacific low-mid tropospheric temperature versus SSTA. (a) MSU2LT V5.2 (closed circle), MSU2LT V5.1 (open circle), NCEP2 (triangle) and ERA40 (cross) (b) AMIP2 simulations (c) 20c3m simulations

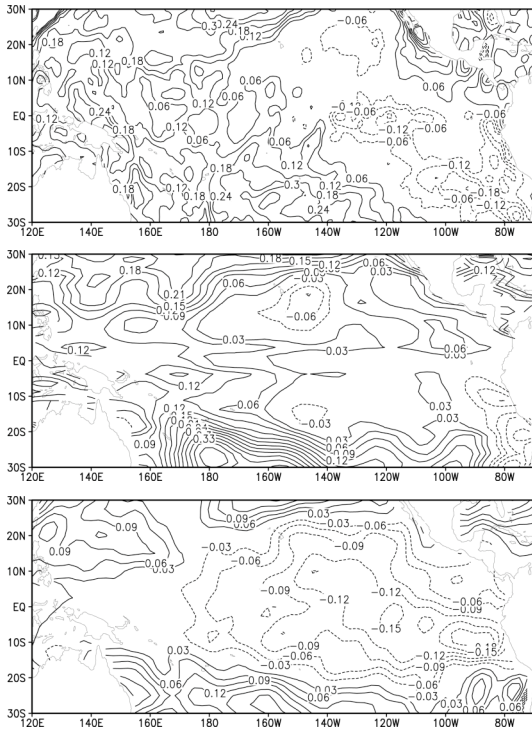


Fig.2 Linear trends in SST (top), MSU2LT V5.2(middle) and MSUE of NCEP2 (bottom)

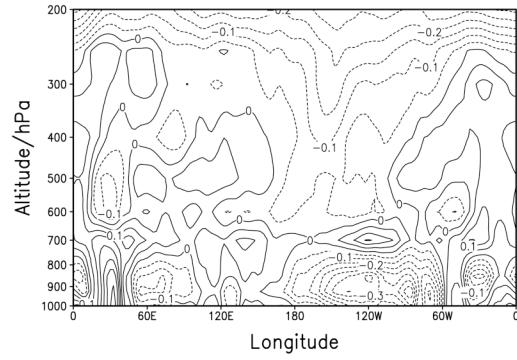


Fig.3 Linear trend in global tropical (20S-20N) tropospheric temperature

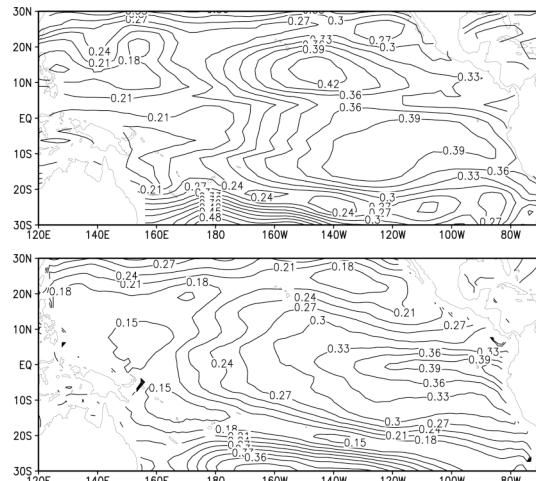


Fig.4 Standard deviations of MSU2LT(top) and MSUE in AMIP2 simulation using CAM (bottom)

Table 1 Trends in SST, MSU 2LT and MSUE 2LT of NCEP2 and ERA40 (K/Dec)

	SST	MSU_2LT	MSU_2LT	NCEP2	ERA40
		V5.1	V5.2		
1979-2004	0.08	-0.023	0.04	-0.04	
1979-1999	0.11	-0.034	0.017	-0.108	-0.013

Table 2 Trends in MSUE of AMIP2 simulations

	CAM3	GISS3	HadGem	ECHAM5
1979-1999	0.106	0.14	0.108	0.108

Table 3 Trends in MSUE (SST) of 20c3m simulations (K/Dec)

	CCSM3	GISS	Hadgem	ECHAM5/OMP	CGCM3.1
1979-1999	0.12 (0.098)	0.14 (0.13)	0.12 (0.085)	0.14 (0.10)	0.26 (0.18)

Evaluation of isotopic variability in an NCAR-CAM3 reanalysis

Vaughan Barras¹, Ian Simmonds¹, David Etheridge², David Noone³

¹ School of Earth Sciences, The University of Melbourne, Parkville, Victoria, Australia

² CSIRO Atmospheric Research, Aspendale, Victoria, Australia

³ PAOS and CIRES, University of Colorado, Boulder, Colorado, USA

An invaluable resource for the modern climate researcher is the information derived from global reanalysis products that provide a vast array of observational atmospheric data assimilated onto regular gridded fields. The coverage over the relatively poorly observed southern hemisphere is of particular interest given that there is a greater dependence in this region upon the assimilation algorithms being used.

A model that routinely incorporates reanalysis data is a version of NCAR-CAM3 that has recently been fitted with an isotopic module (Noone, personal communication). The scheme simulates the fractionation of the stable water isotopes H_2^{18}O and $^1\text{H}^2\text{HO}$ during phase changes throughout the hydrological cycle. The relative abundance of these stable isotopes are useful tracers of moisture history and atmospheric circulation within the model.

As part of a broader study of isotopic variability across southeastern Australia, a special run of NCAR-CAM3 was performed for a period during which rainfall amount and isotopic composition was sampled by the Melbourne University Network of Isotopes in Precipitation (MUNIP) (Barras et al. 2005). This provided an opportunity to test the reanalysis output on a local scale against the detailed observations taken during June 9, 2004. The model was initialised with initial conditions from the NCEP/NCAR reanalysis (Kalnay et al. 1996) and run at a resolution of T42L28 for 6 hours before an adjustment of the atmospheric circulation towards the reanalysis fields and so on.

The rain event over southeastern Australia on June 9, 2004 was characterised by a period of steady rainfall during the day followed by an outbreak of severe storms ahead of a cold front that passed over Melbourne during the late evening. The storms formed with the development of a low pressure system slightly eastwards of the main front with the advection of cold air aloft (Fig. 1a). A comparison of the mean sea level pressure field for this period shows that the subtlety of the circulation observed over southeastern Australia does not seem to be captured by the NCAR-CAM3 model (Fig. 1b). The effect of this is that NCAR-CAM3 maintains continuous stratiform precipitation throughout the entire event.

Model output was also obtained at 20 minute intervals for a column of 3×3 gridpoints centred over a 'Melbourne' gridpoint (37S 145E) to resemble the sampling times of the MUNIP observations. The observations of $\delta^{18}\text{O}$ show a clear separation between the stratiform and convective precipitation (Fig. 2a). There are a number of small scale effects contributing to the variability of these observations, however a more gradual depletion of the stratiform rainfall is noticeable in the earlier samples when compared to the later samples of convective rainfall. The gradual depletion of the simulated isotopes (Fig. 2b) resembles the early stratiform rainfall of the MUNIP observations and this trend remains throughout the period. Despite the lack of fine detail, the simulated variability of isotopes in precipitation for this event is very good given the relatively coarse resolution of NCAR-CAM3 being applied to such a restricted area.

References

Barras V., I. Simmonds and D. Etheridge, Moisture transport across south eastern Australia using stable isotopes in precipitation, in *Research activities in atmospheric and oceanic modelling*, J.Côté (Ed.), Report No. 35, 2.01-2.02, 2005.

Kalnay E. et al., The NCEP/NCAR 40-year reanalysis project, *Bull. Amer. Met. Soc.*, **77**, 437-471, 1996.

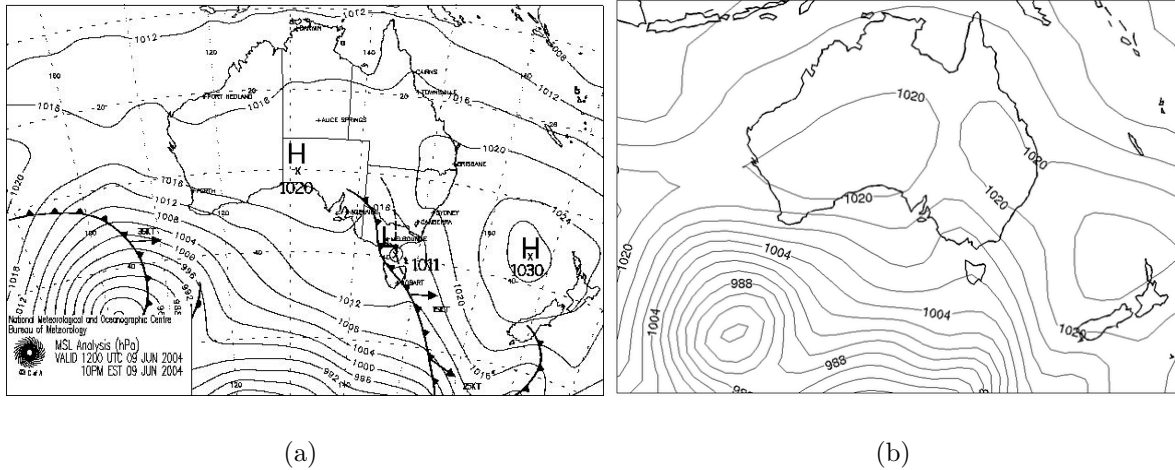


Figure 1: Mean sea level pressure charts for June 9, 2004 valid at 12UTC (22:00 AEST) (a) analysis from observations (courtesy Australian Bureau of Meteorology) (b) NCAR-CAM3 reanalysis.

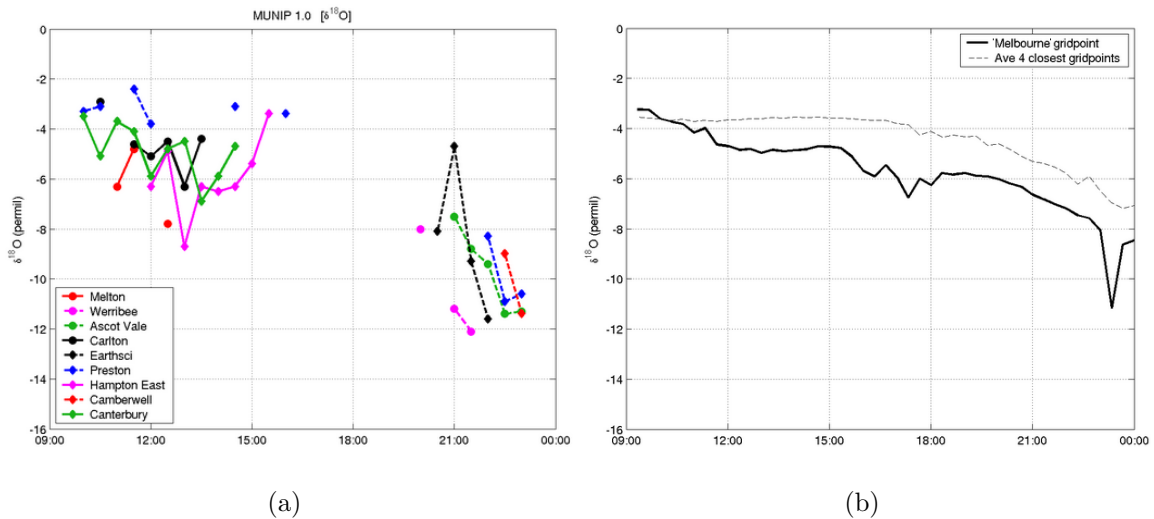


Figure 2: $\delta^{18}\text{O}$ in precipitation for June 9, 2004 from (a) MUNIP sample observations and (b) 20 minute output from NCAR-CAM3 isotope scheme. Local times are indicated (AEST).

Variations in the relative humidity budget from the NCAR/NCEP Reanalysis from 1979-2004

Derek Brown and David Noone

*Cooperative Institute for Research in Environmental Sciences (CIRES),
University of Colorado at Boulder (email: derek.brown@colorado.edu)*

Relative humidity (RH) of an air parcel varies by changing the amount of moisture within the parcel or by changing the saturation vapor pressure. Dynamic processes in the atmosphere can bring about changes in temperature and moisture and thus RH, and warrants the use of RH as a useful diagnostic. The water vapor feedback is central to understanding climate change since constant relative humidity in model simulations of global warming indicate positive water vapor feedback on temperature, while increases in RH can lead to a net negative feedback via cloud effects (e.g., Held and Soden, 2000). Indeed, Lindzen (1990) found that diminished cirrus clouds resulting from convective detrainment with increasing temperature produced less greenhouse heating associated with clouds and that the strength of this negative feedback is at least equal to the positive feedback associated with greenhouse warming due to water vapor. Hall and Manabe (1999) point to the relationship between water vapor and temperature as key in understanding the future of greenhouse-gas induced hydrologic cycle intensification. A more precise understanding of the relationship between moisture and temperature is needed before the role of RH in climate models and on global precipitation anomalies during global climate shifts is appreciated.

RH can be approximated by the ratio of specific humidity to the saturation specific humidity, as $H = e/e_s \approx q/q_s$. Using the Clausius-Clapeyron equation at constant pressure, one can show

$$d \ln H = d \ln q - \left(\frac{L}{R_v T} \right) d \ln T. \quad (1)$$

Peixoto and Oort (1996) showed that on constant pressure surfaces, temperature changes are 20 times more effective at changing RH values than are changes in moisture. However, since moisture is more variable than temperature, both moisture and temperature become important in changing RH values. The humidity, wind and temperature fields from the NCEP reanalysis were used to decompose the time mean budgets for relative humidity into contributions from condensation, advection (both eddy and zonal mean components), adiabatic work, and diabatic heating as they appear in the budget equations for both specific humidity and temperature that appear in equation (1).

Figure 1 shows the variability of dominant terms in the RH budget over the northern midlatitudes. RH changes brought about by zonal mean divergence and adiabatic work correlate with the ENSO events, while latent heating effects to RH remain fairly constant over time. Moisture induced RH changes in the northern midlatitudes vary with zonal mean and eddy moisture divergence, as well as with condensation (or evaporation). Additionally, RH changes by eddy moisture divergence appear to govern RH changes associated with condensation. For the northern subtropical region, **Figure 2** shows the zonal mean heat divergence, heating by adiabatic work and latent heat release to be central to producing interannual variability in RH. For moisture variability, the zonal mean circulation counters RH changes induced by condensation.

The different terms important for the two regions' RH budgets are indicative of the trends in circulation patterns. For instance, in 1998, a strong El Nino event caused the northern midlatitudes to have increased heat and moisture convergence by the zonal mean resulting in RH fluctuations. In the northern subtropics, the convergence of cool, dry air during this same year, combined with the additional effect of increased latent heating, drove decreases in RH values. As such, because variations in moisture and temperature are associated with the global atmospheric circulation, RH values give a diagnostic view of first order hydrologic balance as well as insight into the atmospheric circulation.

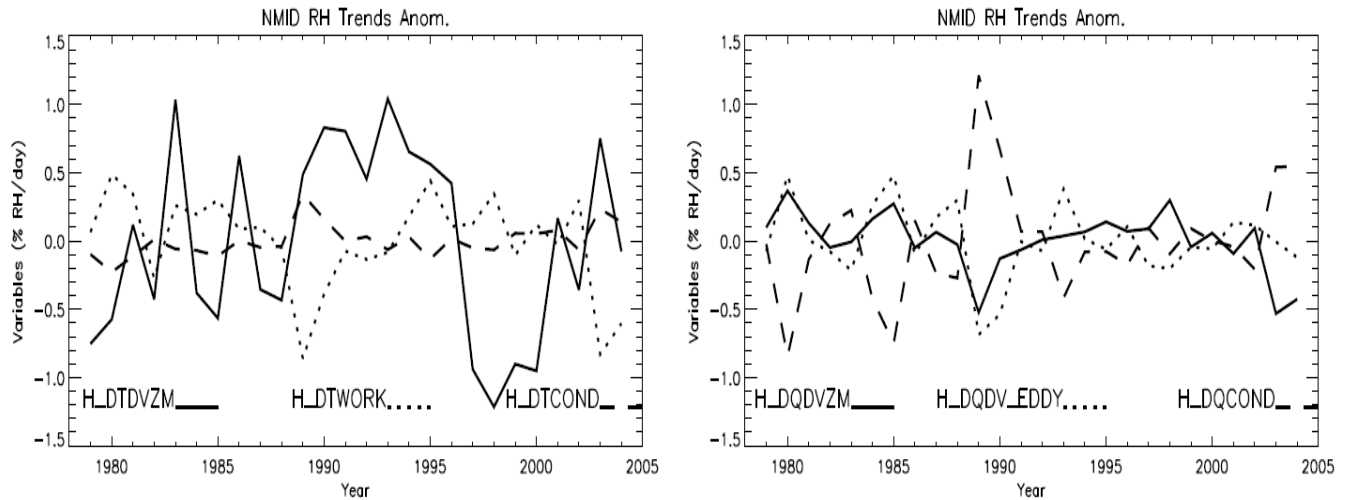


Figure 1: The dominant heating (left) and moisture (right) terms for the zonally averaged, mass weighted relative humidity budget over the northern midlatitudes (40-55N, 500-925hPa). Terms shown are changes in RH due to both meridional and vertical heat divergence by the zonal mean (H_DTDVZM), adiabatic compression or expansion (H_DTWORK), latent heating (H_DTCOND), to moisture divergence by the zonal mean (H_DQDVZM), moisture divergence by eddies (H_DQDV_EDDY) and net condensation (H_DQCOND).

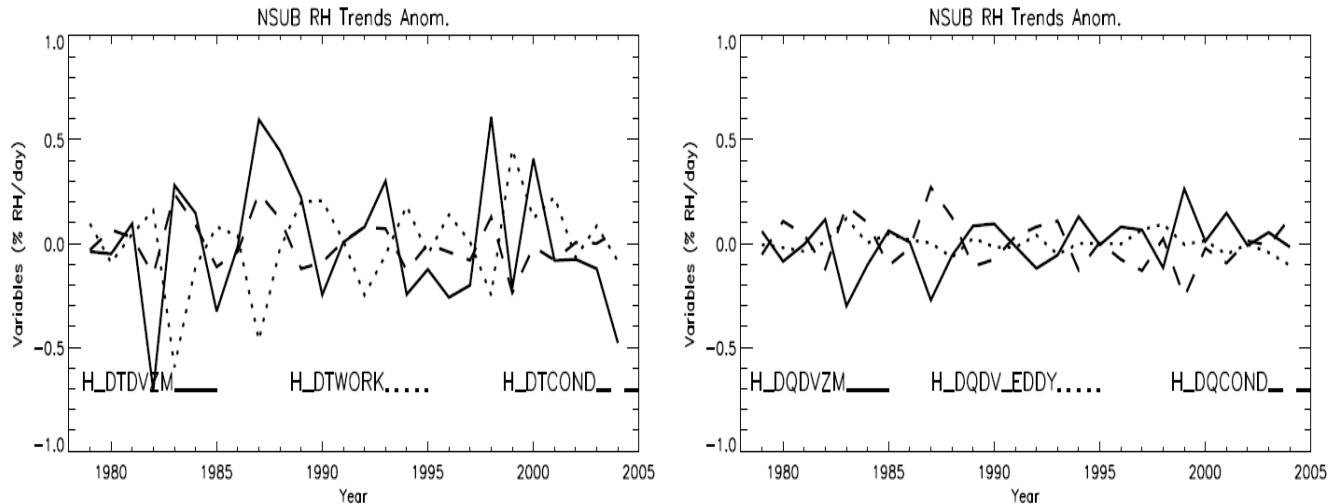


Figure 2: As in Figure 1 but for the northern subtropics (10-35N, 500-925hPa).

Hall A. and Manabe S. 1999: The Role of Water Vapor Feedback in Unperturbed Climate Variability and Global Warming. *Journal of Climate*, **12**, 2327-2346.

Lindzen R. 1990: Some coolness concerning global warming. *Bulletin of the American Meteorological Society*, **71**(3), 288-299.

Peixoto J. and Oort A. 1996: The Climatology of Relative Humidity in the Atmosphere. *Journal of Climate*, **9**, 3443-3463.

Held I. and Soden B. 2000: Water Vapor Feedback and Global Warming. *Annual Review of Energy in the Environment*, **25**, 441-475.

Global and regional cloudiness changes by satellite data: Relationship with temperature and El Nino effects

A.V. Chernokulsky and I.I. Mokhov

A.M. Obukhov Institute of Atmospheric Physics RAS, Moscow, Russia

chern_av@ifaran.ru

There is uncertainty in the sign of changes in cloudiness accompanying global temperature changes (global warming, in particular) from observations and simulations (Mokhov and Chernokulsky, 2003). We present estimates of the relationship between cloudiness from ISCCP data (Rossow and Duenas, 2004) and surface air temperature (Parker et al., 2004) for the Northern and Southern Hemispheres for the period 1983-2004. Both for annual mean regime, and for various seasons regions dominate with negative trends of total cloud amount and negative correlation between cloudiness and surface air temperature. (Table 1, 2).

Positive trends of total cloud amount and positive correlation between total cloud amount and surface air temperature have been revealed in some regions: mid-latitude belt of Eurasia; subtropical and middle latitudes of Northern America, Australia, Aleutian Low and the El Nino formation regions.

Table 1. Trends of annual-mean cloudiness and corresponding coefficient of correlation

Averaging zone		Trend (Year ⁻¹) ± standard deviation	Coefficient of correlation
With polar latitudes (90°S – 90°N)	Land + Ocean	-0.0018 ± 0.0002	-0.89
	Ocean	-0.0019 ± 0.0003	-0.88
	Land	-0.0016 ± 0.0002	-0.86
Without polar latitudes (60°S – 60°N)	Land + Ocean	-0.0020 ± 0.0003	-0.88
	Ocean	-0.0021 ± 0.0003	-0.88
	Land	-0.0017 ± 0.0003	-0.82
Tropical latitudes (30°S – 30°N)	Land + Ocean	-0.0028 ± 0.0003	-0.91
	Ocean	-0.0030 ± 0.0004	-0.90
	Land	-0.0022 ± 0.0003	-0.86

Table 2. Results of linear regression of cloudiness to temperature

Averaging zone		Coefficient of regression (K ⁻¹) ± standard deviation	Coefficient of correlation
With polar latitudes (90°S – 90°N)	Land + Ocean	-0.054 ± 0.015	-0.68
	Ocean	-0.059 ± 0.017	-0.68
	Land	-0.043 ± 0.015	-0.59
Without polar latitudes (60°S – 60°N)	Land + Ocean	-0.062 ± 0.018	-0.67
	Ocean	-0.066 ± 0.018	-0.68
	Land	-0.048 ± 0.017	-0.58
Tropical latitudes (30°S – 30°N)	Land + Ocean	-0.088 ± 0.022	-0.71
	Ocean	-0.095 ± 0.025	-0.70
	Land	-0.066 ± 0.021	-0.63

It should be noted, that significant uncertainty of spatial distribution and temporal changes of cloudiness can be related with nonhomogeneity of ISCCP data.

Relationship between interannual variations of cloudiness and El Nino events has been analyzed. The most significant differences in cloudiness between El Nino phases (years with largest positive anomalies of Nino 3 SST (5°N-5°S 150°W-120°W)) and La Nina phases

(years with largest negative anomalies of Nino 3 SST) are noted over equatorial Pacific Ocean (Fig. 1). Statistically significant correlation between sea surface temperature in the Nino3 region and total cloudiness has been noted in subtropical and tropical latitudes in western part of Pacific Ocean (positive correlation) and in equatorial latitudes of Pacific Ocean (negative correlation) (Fig. 2).

Figure 1. Difference for cloudiness in December-January-February between 5-year-means with largest positive (1986-87, 1991-92, 1994-95, 1997-98, 2002-03) and negative (1984-85, 1985-86, 1989-90, 1998-99, 1999-2000) anomalies of Nino 3 SST.

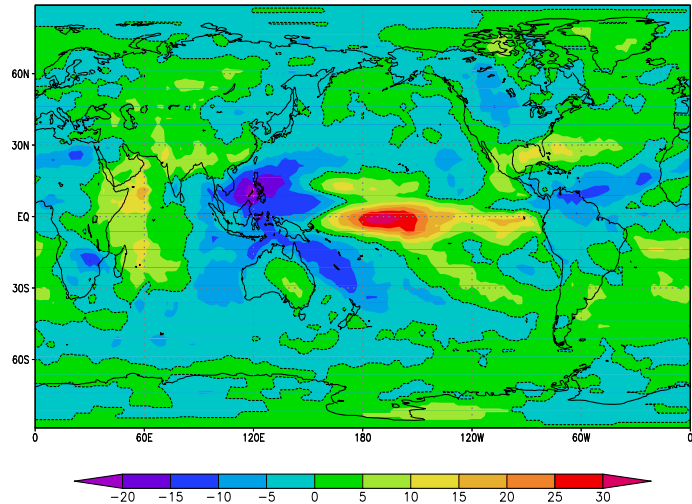
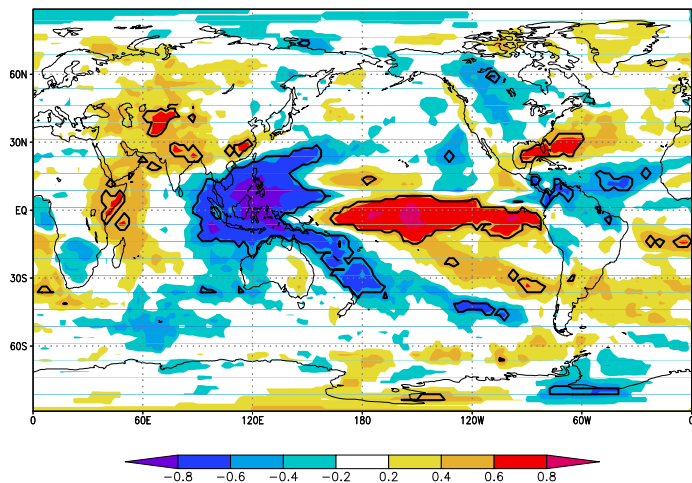


Figure 2. Correlation between cloudiness and Nino 3 SST anomalies in December-January-February (Black thick line: 95% significance level).



This work was partly supported by the Russian Foundation for Basic Research and Program of the Russian Academy of Sciences.

References

- Mokhov, I.I., and A.V. Chernokulsky, 2003: Global cloudiness: Tendencies of Change from ISCCP data. Research Activities in Atmospheric and Oceanic Modelling. J. Cote (ed.). WMO/TD-No.1161, 07.15-07.16.
- Parker, D.E., L.V. Alexander, and J. Kennedy, 2004: Global and regional climate in 2003. *Weather*, **59**, 145-152.
- Rossov, W.B., and E. Duenas, 2004: The International Satellite Cloud Climatology Project (ISCCP) web site: An online resource for research. *Bull. Amer. Meteorol. Soc.* **85**, 167-172.

Some Features of Temperature-Humidity Layering of Troposphere for Different Cloudy Conditions

Irina V. Chernykh

*All Russian Institute of Hydrometeorological Information – Word Data Center, Obninsk, Russia,
E-mail: civ@meteo.ru*

Study of temperature-humidity layering of troposphere (THLT) plays important role in research of atmosphere properties (Fridzon 2004; Chernykh and Aldukhov, 2004; Alduchov et al., 2005; Chernykh et al., 2005). Macro temperature-humidity layering can be visually detected, when such cloud types as stratus, stratocumulus, altostratus, altocumulus, cirrus present. More detailed THLT can be detected by CE-method of analysis of temperature and humidity profiles, obtained during standard radiosonde sounding of atmosphere (Chernykh and Eskridge, 1996; Chernykh and Aldukhov, 2004).

Main goal of this study is to present statistical analysis of THLT detecting by CE-method for different sky condition: with thick and thin cloud layer of stratocumulus, altocumulus and cirrus.

Twice-daily radiosonde sounding data and surface-based cloud observations for 1975-80 period (NCDC, 1991) for eight stations, placed in regions with different climatic conditions are using for this research. The observations with one reported cloud layer were included in this study. Below, opaque part exceeds 50% of the cloud amount (the transparent part is less than 50% of the cloud amount) for thick cloud layers and for thin cloud layers vice versa (NCDC, 1991). In total 6440 cases were used for analysis: 2919 cases of thick and 3521 cases for thin cloud layers.

Percent of correctly diagnosed cloud level (PL) by CE method, percent of diagnosed only observed cloud level (P1) and percent of diagnosed observed cloud level and predicted also higher humid layers (P2) for stratocumulus layer are presented in Table 1. PL for thick stratocumulus layer varies from 85 % to 98 % and for thin - from 71 % to 97 %. Results presented in Table 1 show that for condition with present of thick Sc layer THLT take place not only in low troposphere more often in comparison with thin Sc present. In reality, P1 for thick Sc layer varies from 12 % to 33 % and for thin - from 29 % to 61 %. P2 for thick Sc layer varies from 47 % to 72 % and for thin - from 18 % to 57 %.

TABLE 1. Percent of correctly diagnosed cloud level by CE method, PL.

Percent of diagnosed only observed cloud level, P1. Percent of diagnosed observed cloud level and predicted also higher humid layers (greater than 20% coverage), P2. AV is average cloud cover in the tenth of the sky; N is the number of correspondent observations.

Station	One visible Stratocumulus thick layer					One visible Stratocumulus thin layer				
	PL	P1	P2	AV	N	PL	P1	P2	AV	N
Amarillo	93.6	22.3	63.1	9.6	157	71.8	41.0	20.5	2.5	39
Cape Hatteras	93.9	21.4	62.9	9.3	229	92.4	51.5	33.3	2.9	66
Brownswille	97.5	31.8	61.3	9.5	437	97.1	61.3	34.1	2.7	173
Albany	96.7	23.0	58.0	9.3	538	90.5	44.3	32.4	2.5	210
Spokane	96.8	11.7	72.3	9.5	94	86.4	45.5	18.2	2.4	22
Medford	97.9	32.8	58.4	9.3	341	89.6	52.2	32.8	2.9	67
Ele	85.2	19.0	46.5	8.8	142	72.3	38.3	26.6	2.9	94
Point Barrow	97.4	27.9	64.4	9.6	233	93.5	29.0	56.5	3.5	62

The same results for altocumulus layers are shown in Table 2. In additional percent of diagnosed observed cloud level and predicted also underlying moist layers (greater than 20% coverage and less than 600 m in total thickness), P3, is presented in Table 2. PL for thick altocumulus layer varies from 89 % to 100 % and for thin - from 89 % to 99 %. The results of this table show that THLT take place also in low and high troposphere more often for condition with present thick Ac layer in comparison with present thin Ac layer. In reality, P1 for thick Ac layer varies from 4 % to 29 % and for thin - from 6 % to 46 %. P2 for thick Ac layer varies from 9 % to 23 % and for thin - from 3 % to 14 %. P3 for thick Ac layer varies from 39 % to 84 % and for thin - from 34 % to 87 %.

Results for thin cirrus layers are shown in Table 3. PL for thin cirrus layer varies from 77 % to 99 %. P1 for thin Ci layer varies from 5 % to 22 % and P3 varies from 71 % to 88 %.

TABLE 2 is the same as TABLE 1, but for Altocumulus.
P3 - percent of diagnosed observed cloud level and predicted also underlying moist layers (greater than 20% coverage and less than 600 m in total thickness).

Station	One visible Altocumulus thick layer						One visible Altocumulus thin layer					
	PL	P1	P2	P3	AV	N	PL	P1	P2	P3	AV	N
Amarillo	92.2	21.6	21.6	41.2	8.9	102	97.0	43.9	12.1	37.9	2.3	66
Cape Hatteras	94.7	7.1	15.9	68.2	9.4	170	89.1	20.0	5.5	60.0	2.8	55
Brownswille	89.2	11.7	14.4	61.3	8.9	111	96.6	10.3	13.8	72.4	2.6	29
Albany	100	25.9	14.8	55.6	8.7	54	96.9	32.3	3.1	58.5	2.2	65
Spokane	99.1	23.0	11.5	59.3	8.9	113	98.5	25.9	7.4	61.5	2.4	135
Medford	95.8	15.3	17.8	60.2	9.4	118	96.6	32.8	13.8	48.3	2.5	58
Ele	96.8	29.0	22.6	38.7	8.7	31	96.9	46.2	9.2	33.8	2.8	65
Point Barrow	97.8	4.4	8.9	84.4	9.2	45	98.1	5.7	5.7	86.8	3.0	53

TABLE 3 is the same as TABLE 1, but for Cirrus thin layers.

Station	One visible Cirrus thin layer				
	PL	P1	P3	AV	N
Amarillo	98.6	21.0	76.6	3.9	499
Cape Hatteras	94.1	16.5	77.6	3.8	473
Brownswille	96.9	15.4	81.5	3.8	259
Albany	97.9	9.7	88.3	3.0	145
Spokane	95.8	16.3	79.6	4.3	289
Medford	95.9	21.6	74.3	4.0	222
Ele	92.3	9.7	82.6	4.0	298
Point Barrow	76.6	5.2	71.4	3.5	77

Conclusions: THLT can be detected on base radiosonde sounding data by CE method; temperature-humidity layering of troposphere takes place for different sky condition; thick and thin cloud layers are only visible part of the temperature-humidity layering of troposphere.

Results can be used for modeling of atmospheric circulation and cloud modeling.

Acknowledgment. Study was partly supported by Russian Basic Research Foundation (RBRF), project № 04-05-64681.

REFERENCES

- Alduchov O.A., Aggarwal P.K., I.V. Chernykh, 2005: Isotope Ratios in Precipitation and Some Key Upper-Air of the Boundary Layer. Program and Abstract Book 5th International Scientific Conference on the Global Energy and Water Cycle. GEWEX WCRP. 20-24 June 2005. Costa Mesa, California. P. 206.
- Chernykh I.V., Aggarwal P.K., O.A. Alduchov, 2005: About Correlations of Isotope Ratios and Clouds Parameters. Program and Abstracts Book 5th International Scientific Conference on the Global Energy and Water Cycle. GEWEX WCRP. 20-24 June 2005. Costa Mesa, California. P. 210.
- Chernykh I.V. and R.E. Eskridge, 1996: Determination of cloud amount and level from radiosonde soundings. *J. Appl. Meteorol.*, **35**, 1362-1369 pp.
- Chernykh I.V. and O.A. Alduchov, 2004: Vertical Distribution of Cloud Layers from Cloud Radiosounding Data. *Izvestiya, Atmospheric and Oceanic Physics*. Vol. 40, No 1, 2-004, pp. 41-53.
- Fridzon M.B., 2004: Methods of electromagnetic transmission probing of atmosphere and reliability of measurements of temperature and humidity at altitudes up to 35-40 km. Doctoral Dissertation in Technics. Moscow. 2004.
- NCDC, 1991: TD-3280 Surface Airways Hourly. Internal Report of the National Climate Data Center, 40pp.

Relationships between the Maritime Continent and the Walker Circulation

Katherine E. Dayem^{1*}, David C. Noone², Peter Molnar¹

1. Department of Geological Sciences and CIRES, University of Colorado, Campus Box 399, Boulder, CO, 80309.
2. Program in Atmospheric and Oceanic Sciences and CIRES, University of Colorado, Campus Box 311, Boulder, CO, 80309 *email: dayem@colorado.edu

The existence of the islands of the Maritime Continent in the western Pacific Ocean has a profound effect on tropical atmospheric circulation. The Walker Circulation, which is made up of ascent over the western Pacific, descent over the central Pacific, and upper-level westerlies and surface easterlies over the Pacific, may be enhanced by atmospheric heating over the Maritime Continent. The amount of land surface area of the Maritime Continent has increased in the past ~3-4 million years in large part because New Guinea has moved northward into the tropics (Cane and Molnar, 2001). A change in tropical climate also occurred ~3-4 Ma. Prior to this time, a permanent El Niño state is thought to have persisted in the Pacific Ocean (Cane and Molnar, 2001). A steepened thermocline and increase in SST gradient across the Pacific Ocean lead to a change to the El Niño – Southern Oscillation state of present day (Ravelo *et al.*, 2004; Wara *et al.*, 2005).

We analyze 5 years of precipitation rate data over the Maritime Continent and Western Pacific Warm Pool from the Tropical Rainfall Measurement Mission (TRMM) satellite (data product 2B31, which combines measurements from the satellite's precipitation radar and microwave imager) from March 2000 to February 2005. Precipitation rates are largest over central New Guinea, central Borneo, and off the west coast of Sumatra (Dayem *et al.*, 2005). Rates are also large over the warm pool (Figure 1). We correlate average precipitation rate over the Maritime Continent and the warm pool (Figure 1) with u and w from the NCAR/NCEP reanalysis data set. Precipitation rates over both the Maritime Continent and the warm pool correlate positively with w over the western Pacific, indicating enhanced ascent with increased precipitation over these areas (Figure 2). Increased precipitation rates over the Maritime Continent correlate positively with enhanced upper-level westerlies and surface easterlies over the Pacific (enhanced Walker Circulation), but precipitation rates over the warm pool correlate with weakened upper-level westerlies and surface easterlies over the Pacific (suppressed Walker Circulation) (Figure 3). These results suggest that latent heating of the atmosphere over the Maritime Continent is an important feature of the Walker Circulation, but latent heating of the atmosphere over the warm pool is not (Dayem *et al.*, 2005).

We compare GCM simulations (CAM3) without the entire Maritime Continent and without New Guinea to a control simulation with present-day topography. Where land is removed it is replaced by open ocean with a sea surface temperature linearly interpolated from nearby ocean data. Preliminary results indicate that ascent is localized over the islands of the Maritime Continent in the control case, but is spread more evenly across the region when the islands are removed (Figure 4b). When only New Guinea is removed, ascent is reduced over New Guinea's position but is localized over the remaining islands (Figure 5b). Surprisingly, upper-level westerlies are stronger when the Maritime Continent is removed, but surface easterlies are weakened (Figure 4b). Upper-level westerlies are similar in the control and removed New Guinea cases, but surface easterlies are slightly reduced when New Guinea is removed. This suggests that the islands of the Maritime Continent serve to localize ascent, and their presence may be related to a strengthened Walker Circulation.

References

Cane, M.A., and P. Molnar (2001) Closing of the Indonesian seaway as a precursor to east African aridification around 3-4 million years ago, *Nature*, 411, 157-162.

Dayem, K.E., D.C. Noone, and P. Molnar (2005) Tropical Western Pacific Warm Pool and Maritime Continent precipitation rates and their contrasting relationships with the Walker Circulation, *in review*.

Ravelo, A.C., D.H. Andreasen, M. Lyle, A.O. Lyle, and M. W. Wara (2004) Regional climate shifts caused by gradual global cooling in the Pliocene epoch, *Nature*, 429, 263-267.

Wara, M.W., A.C. Ravelo, M.L. Delaney (2005) Permanent El Niño-like conditions during the Pliocene warm period, *Science*, 309, 758-761.

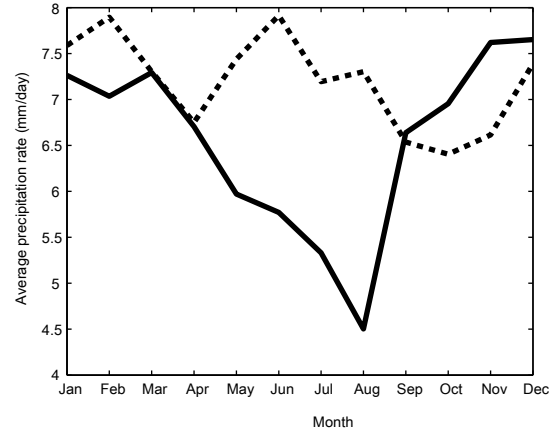


Figure 1: March 2000 - February 2005 monthly average precipitation rate (mm/day) over the Maritime Continent (solid line) and the Warm Pool (dashed line).

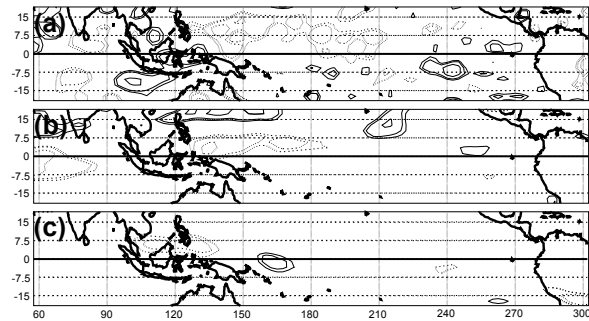


Figure 2: Significance levels of correlation of 5-yr average precipitation rate anomalies over the Maritime Continent with (a) w_a at 850 mb, (b) u_a at 850 mb, and (c) u_a at 250 mb. Contours of 80%, 90%, and 99% confidence are solid (dashed) for positive (negative) correlation.

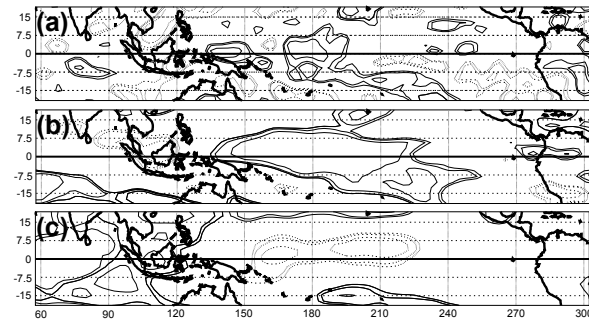


Figure 3: Significance levels of correlation of 5-yr average precipitation rate anomalies over the Warm Pool with (a) w_a at 850 mb, (b) u_a at 850 mb, and (c) u_a at 250 mb. Contours of 80%, 90%, and 99% confidence are solid (dashed) for positive (negative) correlation.

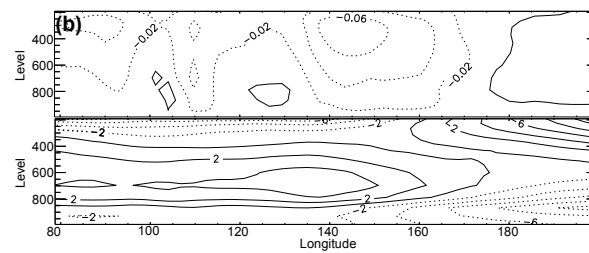
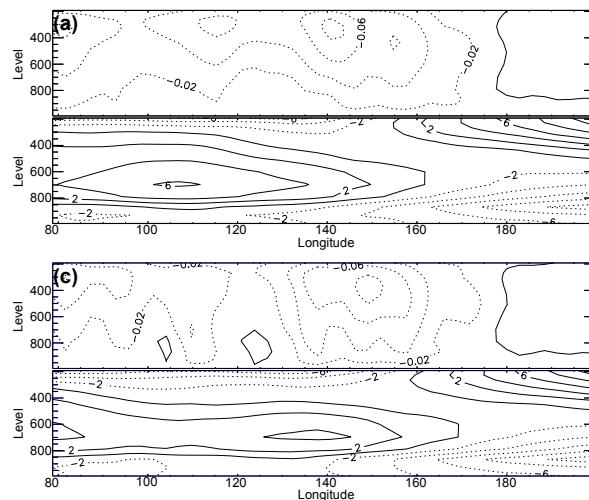


Figure 4: GCM simulation results of (a) run without the Maritime Continent, (b) run without New Guinea, and (c) a control with present-day topography. The top panel shows ω and the bottom show u . Values are averaged over latitudes from 7°S to 7°N.

WGNE assessment of Quantitative Precipitation Forecasts from Operational Numerical Weather Prediction Models over the U.K.

Paul Earnshaw*, Marion Mittermaier and Clive Wilson
Met Office, FitzRoy Road, Exeter, EX1 3PB, UK.

The forecasts of daily precipitation accumulation from the 12 UTC run of 7 global, operational numerical weather prediction models were verified over the U.K. While the exercise has been in progress since 2000, we show results from January 2003 to June 2005 (slightly different samples between models because of transmission problems). The model data were up/down-scaled by box-averaging to a common resolution of $96 \times 96 \text{ km}^2$. The forecasts were compared against upscaled daily accumulations derived from quality controlled and corrected radar observations ([1]) comprising the British Isles and adjacent waters.

The statistics of daily accumulations reaching a set of thresholds has been computed on the basis of monthly and total contingency tables. Plots of Frequency Bias, Odds Ratio and Equitable Threat Score (ETS) are presented.

Figure 1 shows that at the lower end of the threshold range ($\leq 2 \text{ mm day}^{-1}$), all but one model overforecasts the number of events. However, all models show the highest accuracy at these thresholds (from maximum ETS). At the higher thresholds, the tendency for over and underforecasting events is split equally amongst the models. The skill of forecasting the events and the accuracy of the forecasts shows a degree of variation amongst the centres. The models with the higher resolutions and more sophisticated assimilation systems appear to be the better performers in this respect.

While it is not shown, the monthly timeseries of these scores shows a high degree of variability, of which some can be attributed to the seasonal cycle of precipitation over the U.K. The seasonal cycle in the scores shows better forecasting of precipitation during winter than during summer. This is explained by the difference in the type of weather experienced in these seasons, winter is characterised by the more predictable large-scale cyclonic depressions and the summer by less predictable small-scale convective showers. The latter of these two cases is not particularly well forecast by any of the global models where the grid scale is much larger than the convective scale.

References

- [1] D.L. Harrison, S.J. Driscoll, and M. Kitchen. Improving precipitation estimates from weather radar using quality control and correction techniques. *Meteorol. Appl.*, 6:135–144, 2000.

*©British Crown Copyright; email: paul.earnshaw@metoffice.gov.uk

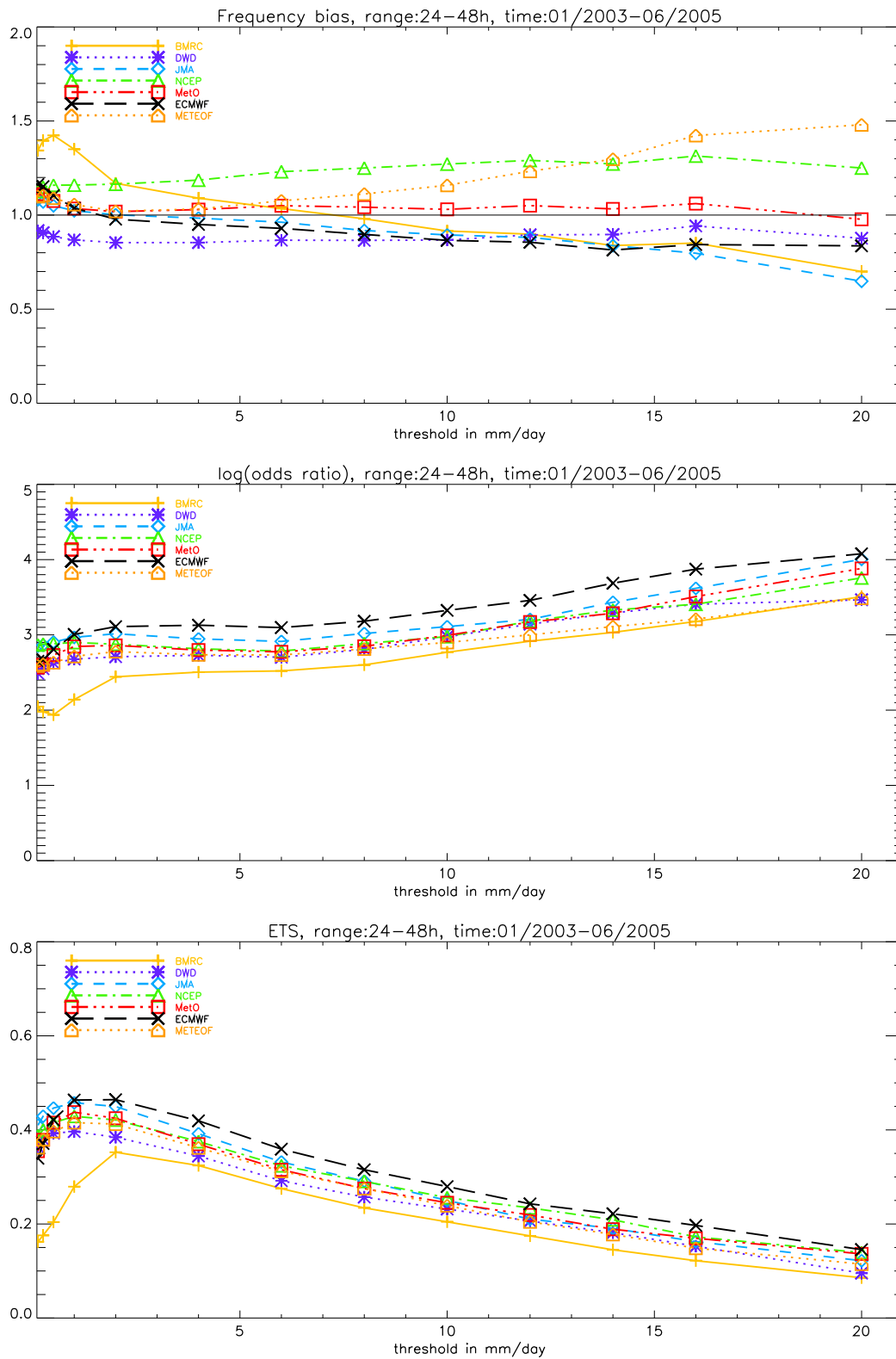


Figure 1: Frequency bias, Log(Odds Ratio) and ETS for the 7 participating centres. The forecast is an accumulation from 24 to 48 hours averaged over the period Jan 2003 to June 2005.

Interdecadal Variability of Surface Heat Fluxes Over the Atlantic Ocean

Paul J. Hughes^{1,2}, Mark A. Bourassa^{1,2}, Jeremy Rolph¹, and Shawn R. Smith¹

1. Center for Ocean-Atmosphere Prediction Studies, Florida State University, Tallahassee, FL 32306-2840
2. Department of Meteorology, Florida State University, Tallahassee, FL 32306-2840
hughes@coaps.fsu.edu

Introduction

The spatial and temporal variability of the surface heat fluxes over the North Atlantic is examined using the new objectively produced FSU3 monthly mean $1^\circ \times 1^\circ$ gridded wind and surface flux product (Pegion et al. 2000, Bourassa et al. 2005). The FSU3 product is derived from in situ ship and buoy observations thus can be used as a comparison for longer time scale modeling studies. The analysis shows that the latent and sensible heat fluxes exhibit a low frequency (basin wide) mode of variability over the North Atlantic Ocean. It is hypothesized that the longer time scale variability is linked to changes in the large scale circulation patterns (meridional pressure gradients) possibly associated with the Atlantic Multidecadal Oscillation (AMO; Schlesinger and Ramankutty 1994, Kerr 2000). The anomalous heat fluxes appear to be forced by fluctuations in mean wind speed.

Results

The leading mode of the latent heat flux depicts a basin-wide spatial pattern where much of the North Atlantic is dominated by positive loadings (Figure 1a). The main (positive) action centers are located over the tropical North Atlantic, Caribbean Sea, Gulf Stream, and regions north of 50°N . The PC time series (Figure 1b) depicts longer time scale variability, suggesting a transition from predominantly positive latent heat flux anomalies to negative values around 1998. Similar spatial (north of 40°N) and temporal patterns are also shown in the leading mode of the sensible heat flux (Figures 1c and 1d).

Time series plots of the monthly anomalies (not shown) reveal the low frequency variability. The surface heat fluxes are shown to transition from primarily positive (negative) to negative (positive) anomalies over the tropical North Atlantic (New England coast) around 1998. The transition is not as evident over the central and higher latitude regions.

The two periods (1982-1997 and 1998-2003) are compared by computing the difference between the overall means. The greatest differences for the latent heat fluxes (Figure 2a) occur over the tropics and higher latitude regions of the North Atlantic with values ranging from 20 Wm^{-2} to greater than 30 Wm^{-2} . The greatest sensible heat flux differences (Figure 2b) are located along the New England coast and high latitude regions (exceeding 16 Wm^{-2}). Differences across the tropics, although much smaller, are still statistically significant. The largest wind speed differences ($\geq 1 \text{ ms}^{-1}$) appear to be located around the periphery of the subtropical high, thus suggesting a response to changes in the meridional pressure gradient (Figure 2c). Figure 3b indicates a slight enhancement of the northeasterly trade winds and midlatitude westerlies during 1982-1997. Conversely, Figure 3c shows a weakening of the large scale circulation patterns during 1998-2003 compared to climatology (Figure 3a).

Acknowledgements. This research is funded by the NOAA Office of Climate Observations and NSF Physical Oceanography.

References

- Bourassa, M. A., R. Romero, S. R. Smith, and J. J. O'Brien, 2005: A new FSU winds climatology. *Journal of Climate*, **18**, 3692-3704.
- Kerr, R.A., 2000: A North Atlantic climate pacemaker for the centuries. *Science*, **288**, 1984-1985.
- Pegion, P.J., M.A. Bourassa, D.M. Legler, and J.J. O'Brien, 2000: Objectively derived daily "winds" from satellite scatterometer data. N.C. *Monthly Weather Review*, **128**, 3150-3168.
- Schlesinger, M.E., and N. Ramankutty, 1994: An oscillation in the global climate system of period 65-70 years. *Nature*, **367**, 723-726.

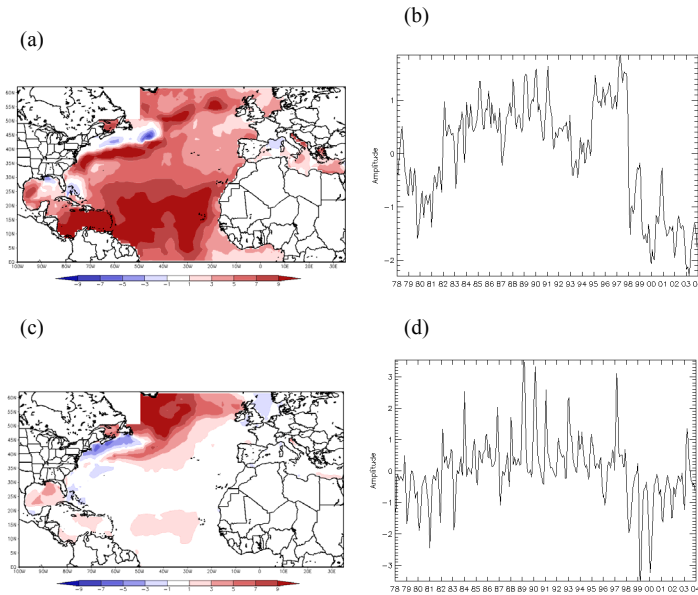


Figure 1. Empirical orthogonal function (EOF) analysis performed on monthly latent and sensible heat flux anomalies (1978-2003). Anomalies filtered (temporally) prior to the EOF analysis. (a) Spatial pattern associated with the leading mode of latent heat flux (~25% variance explained). Loadings are scaled (multiplied by) the standard deviation of the time series. (b) PC time series for mode 1 of latent heat flux. The amplitude values are scaled by dividing through by the standard deviation of the time series. (c) Same as (a) except for sensible heat flux (~21% variance explained). (d) Same as (b) except for sensible heat flux.

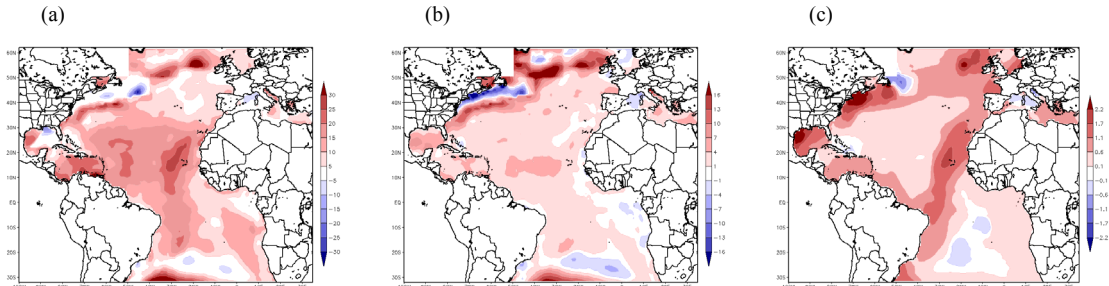


Figure 2. 1982-1997 overall mean minus 1998-2003. (a) Latent heat flux (Wm^{-2}). (b) Sensible heat flux (Wm^{-2}). (c) Wind speed (ms^{-2}). Regions of largest differences were found to be statistically significant at the 95% confidence limit via a two-tailed t test.

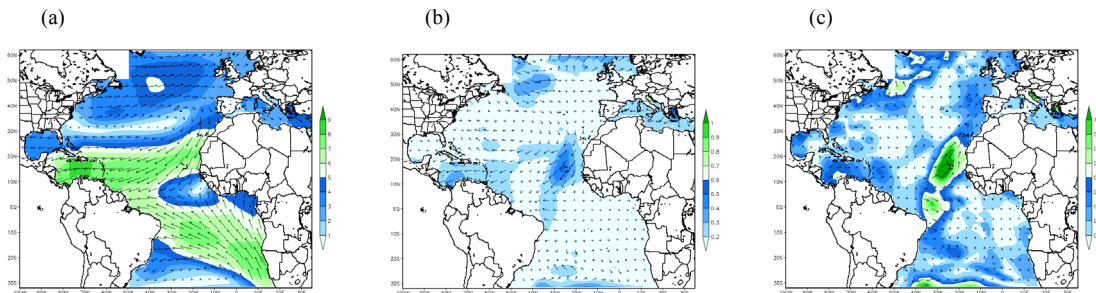


Figure 3. (a) 1978-2003 climatology of vector wind speed (ms^{-1}). (b) Vector wind anomalies for 1982-1997 (ms^{-1}). (c) Vector wind anomalies for 1998-2003 (ms^{-1}).

Intercomparison of deuterium series from the Antarctic stations Vostok and Dome C ice cores

Karpenko A.A.

A.M. Obukhov Institute of Atmospheric Physics RAS
3 Pyzhevsky, 119017 Moscow, Russia
karpenko@ifaran.ru

Intercomparison of the deuterium concentrations in the ice core (D) from the Antarctic stations Vostok (Petit et al., 1999) and Dome C (EPICA, 2004) is performed. The analyzed data (740,000 years for EPICA Dome C and 420,000 years for Vostok) are interpolated linearly to the time step of 500 years. D is a characteristic of temperature (Petit et al., 1999). This analysis gives information about the possible differences between paleoreconstructions from the Vostok and the EPICA Dome C ice core data.

The comparison of the data (Fig.1) shows similarity between of them generally with some differences (Mokhov et al., 2005). Correlation analysis for the last 420,000 years shows synchronous changes of D from Vostok and Dome C and correlation coefficient $r = 0.68$. Correlation analysis with 100,000 year sliding time intervals (Fig.2) shows differences in time dating between EPICA Dome C and Vostok data. The lags for maximum correlation between the data are about 500 years (1 time step) for 0-114 kyr BP (EPICA Dome C data lead), 2500 years (6 time steps) for 114-245 kyr BP (Vostok data lead), and 3500 years (7 time steps) for 245-330 kyr BP (EPICA Dome C data lead). Low r_{\max} for the time intervals 10-115 kyr BP and 145-320 kyr BP indicate the EPICA Dome C and Vostok dating posses are quite different for those time intervals. Different dating between the EPICA Dome C and Vostok data for the time interval 330-420 kyr BP are about 10-11.5 kyr (pretty large), and also this difference is clearly seen from in Fig.1.

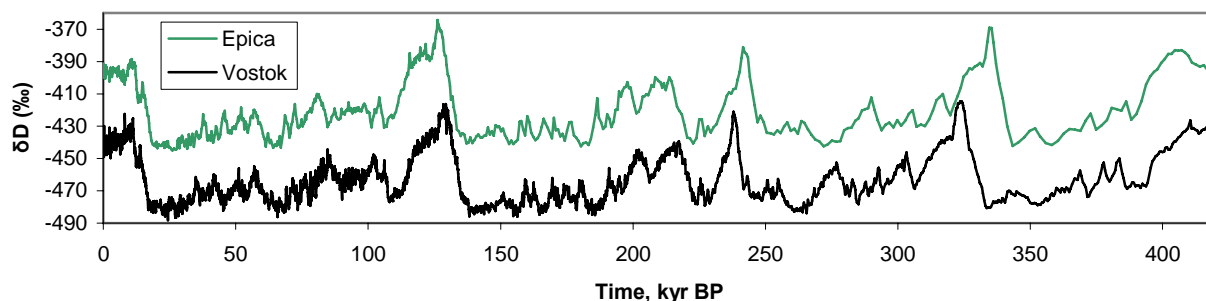


Fig.1. Comparison of the EPICA Dome C data with the Vostok data.

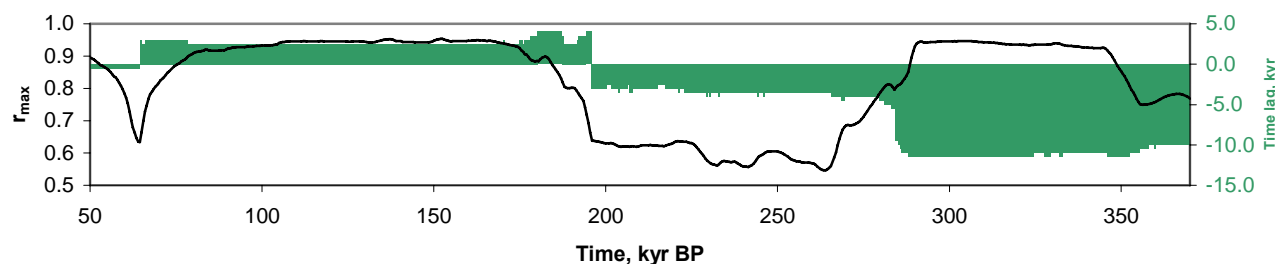


Fig.2. Correlation analysis of the EPICA Dome C data and the Vostok data. The black line shows maximum coefficients of correlation r_{\max} for 100 kyr sliding time interval, and the green area shows the corresponding time lag for r_{\max} (plus – Vostok data lead, minus – EPICA Dome C data lead).

The results of the wavelet analysis (Torrence and Compo, 1998) in Fig.3 show close similarity between the EPICA Dome C and Vostok data (maxima are displayed for about 20, 40 and 100 kyr periods) with some differences in particular for 40 and 20 kyr periods (Mokhov et al., 2005). The spectral peaks for 20, 40 and 100 kyr periods are more significant for EPICA data than for the Vostok data.

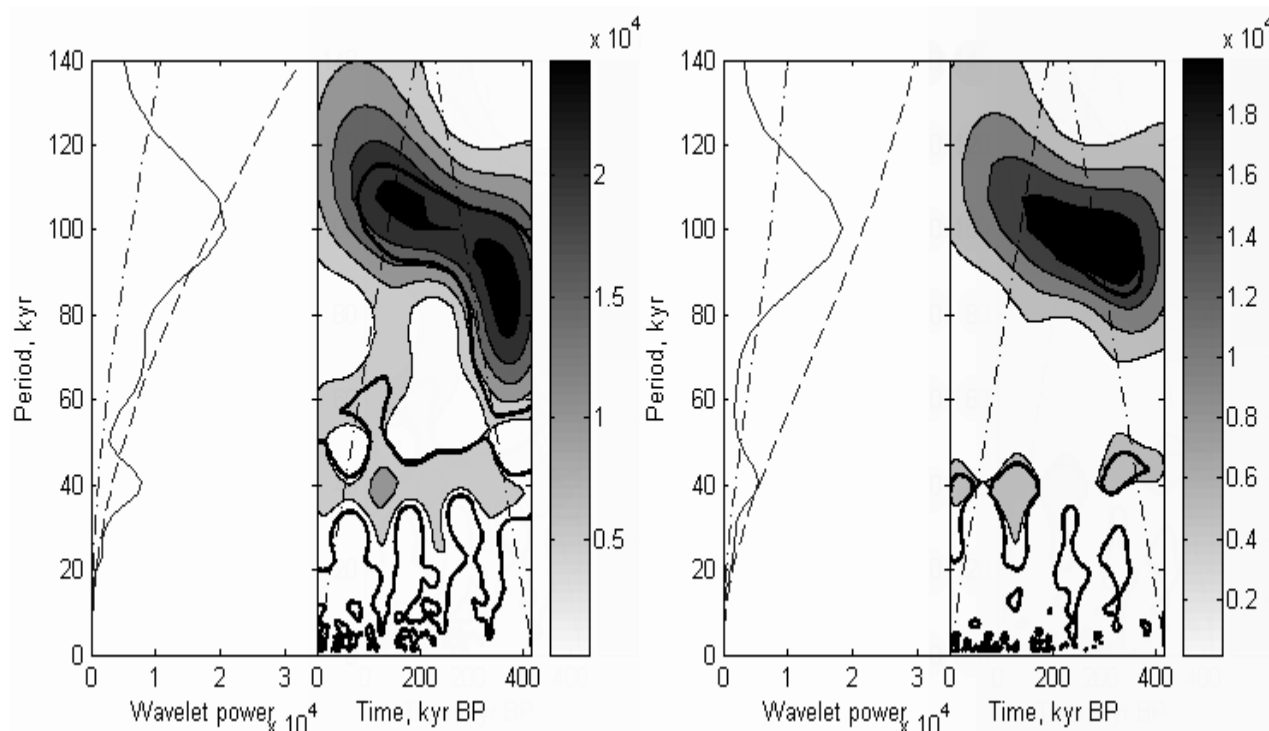


Fig.3. Wavelet analysis of the EPICA deuterium data (left pic) and the Vostok data (right pic).

The EPICA Dome C data show good correspondence with the Vostok data; however the EPICA Dome C data need further time dating improvements.

This work was partly supported by the Russian Foundation for Basic Research.

References

1. Petit, J.R., J. Jouzel, D. Raynaud et al., 1999: Climate and atmospheric history of the past 420000 years from the Vostok ice core, Antarctica. *Nature*, V.399, P.429-436.
2. EPICA community members. Eight glacial cycles from an Antarctic ice core // *Nature*. 2004.V.429. P.623-628.
3. Mokhov I.I., Bezverkhni V.A., Karpenko V.A., Diagnosis of Relative Variations in Atmospheric Greenhouse Gas Contents and Temperature from Vostok Antarctic Ice Core Paleoreconstructions // *Izv., Atmospheric and Oceanic Physic*, 2005, V.41, N.5, P.523-592.
4. Torrence C., Compo G.P. A practical guide to wavelet analysis // *Bull. Am. Meteorol. Soc.* 1998. V.79. P.1906-1931.

Trends in 500 hPa cyclone characteristics and baroclinicity in the Southern Hemisphere winter in 1979-2004

Eun-Pa Lim and Ian Simmonds
School of Earth Sciences
The University of Melbourne
Victoria 3010, Australia
E-mail: eplim@earthsci.unimelb.edu.au

Extratropical cyclones comprise daily weather patterns in the mid and high latitudes and redistribute energy, momentum and moisture across the globe. Therefore, it is important to understand the responses of these extratropical cyclones to recent changes in climate. In this study, we will examine the trends in 500 hPa level cyclone frequency, intensity, and scale over the last 26 years with updated NCEP-DOE reanalysis II data up to 2004. 500 hPa geopotential height (Z500) June-July-August data are used with the application of the Melbourne University cyclone finding and tracking scheme to detect Z500 cyclone tracks (Keable et al. 2002).

Figure 1 shows that Z500 cyclones have increased in their number and intensity in 1979-2004, and their trends are statistically significant at the 95% confidence level. In particular, it is noted that the positive trend of Z500 cyclone frequency is contributed by the increases in the late 1990s and the early 2000s (Figure 1 (a)). On the contrary, the scale of Z500 cyclones experienced sudden reduction in the same period despite the positive trend up to the mid 1990s (Figure 1 (b)). For these interesting changes, one of the causative mechanisms might be found in the change of the static stability measured by the square of the the Brunt-Väisälä frequency (N^2) at the 500 hPa level. Figure 2 (a) shows that the static stability between the 300 and 700 hPa levels has significantly decreased in the mid and high latitudes, and the decrease has accelerated in the last decade (Figure 2 (b)). According to the baroclinic instability theory in Charney's model (Pedlosky 1987), the critical horizontal wavelength of the order of the deformation radius for baroclinic energy release depends on the vertical scale of the disturbance. In the case that the vertical scale of a disturbance, h , is greater than the density scale height, H , the critical horizontal wavelength of the disturbance, L , is determined by

$$L = \frac{NH}{f} \quad (1)$$

where f is the Coriolis parameter. As h is greater than H over most of the SH extratropics at the 500 hPa level (not shown), reduction in N would correspond to the reduction in cyclone scale. At the same time, baroclinicity is inversely proportional to N (Hoskins and Valdes 1990), so this reduction would play a role in enhancing the baroclinicity at this level and contribute to the increase in Z500 cyclone frequency. Such crucial role of the static stability in determining the wavelength of baroclinic wave was shown in the model experiment of Stanley and Gall (1977). On the other hand, the increase of cyclone intensity shown in Figure 1 (c) is consistent with the result of Keable et al. (2002) and also suggest that the change shown in their study has continued in the late 1990s and the early 2000s.

Hoskins, B. J. and Valdes, P. J. (1990). On the existence of storm-tracks, *J. Atmos. Sci.*, **47**, 1854-1864.

Keable, M., Simmonds, I. and Keay, K. (2002). Distribution and temporal variability of 500 hPa cyclone characteristics in the Southern Hemisphere, *Int. J. Climatol.*, **22**, 131-150.

Pedlosky, J. (1987). *Geophysical fluid dynamics*, New York: Springer-Verlag. 710 pp.

Stanley, D. O. and Gall, R. L. (1997). On the wavelength of maximum baroclinic instability, *J. Atmos. Sci.*, **34**, 1679-1688.

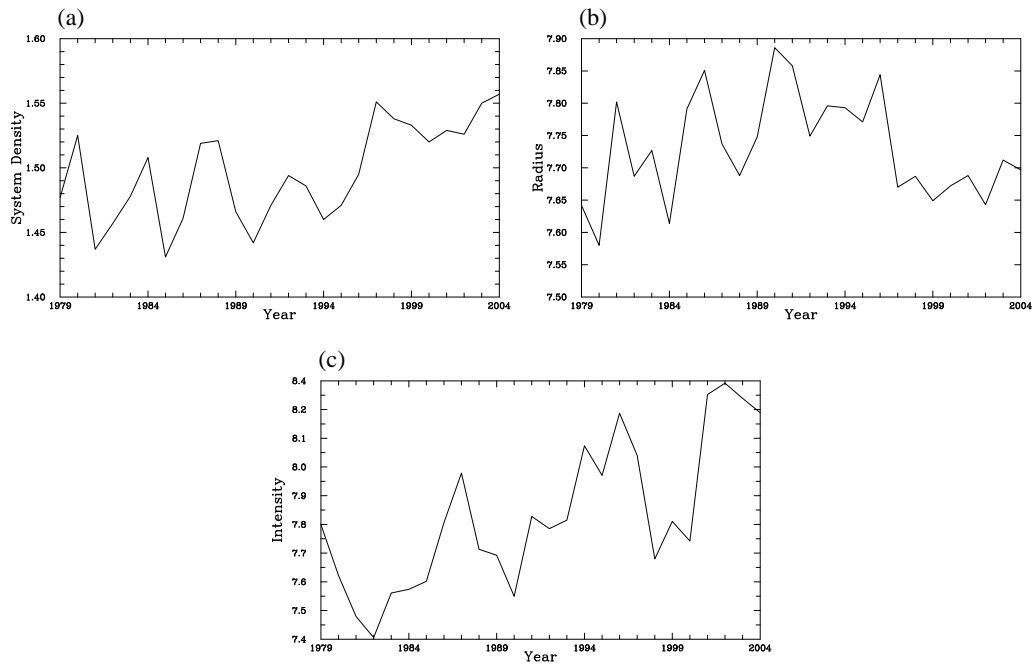


Figure 1: Time series of SH winter zonal averages of Z500 cyclone properties (a) system density (the number of cyclones over in 10^3 ($^\circ$ lat) 2), (b) radius ($^\circ$ lat), and (c) intensity ($\text{m } (^\circ \text{ lat})^{-2}$).

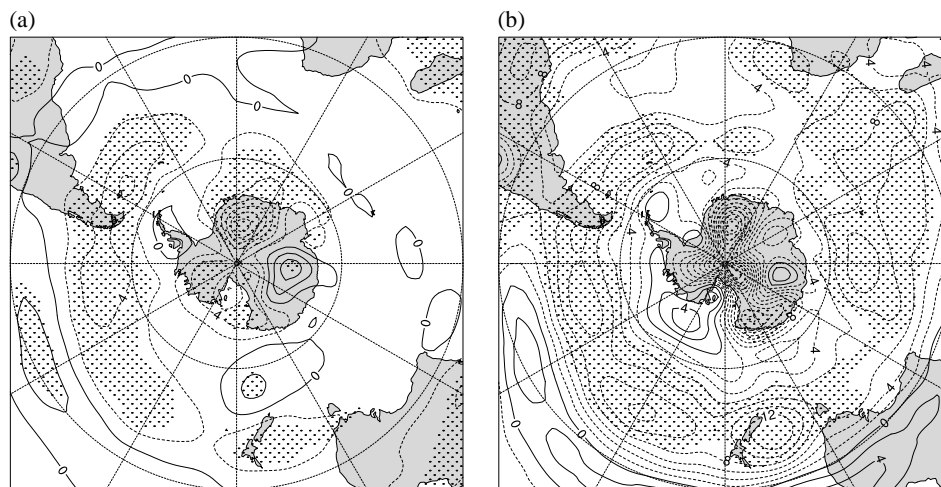


Figure 2: Trend of N^2 at the 500 hPa level in (a) 1979-2004 and (b) 1991-2004. The contour interval is $2 \times 10^{-6} \text{ s}^{-2} \text{ decade}^{-1}$.

Assessment of precipitation forecasts from operational NWP models over the UK

Marion Mittermaier*

Mesoscale model development and diagnostics, NWP, Met Office, FitzRoy Road, Exeter, EX1 3PB, UK

During 2004 an European model intercomparison of precipitation forecasts was begun, with the 10 km ALADIN (Meteo France), the 7 km Lokall Model (LM) from the DWD, the 22 km reference HIRLAM (FMI) and the 12 km mesoscale Unified Model (MES). Early in 2005 the 7 km MeteoSwiss version of the LM, aLMo was also added to the comparison. The aLMo is different to the LM as it uses ECMWF boundary and initial conditions. The contributing weather services have password-protected access to a web page hosted by the Met Office where the monthly results are posted. The intercomparison aims to verify the daily accumulations produced by the various models against the UK NIMROD radar-rainfall composite over a large part of the UK. At present the 00Z runs are compared. All the models as well as the 5 km by 5 km radar composites are upscaled to the 22 km HIRLAM grid.

Figure 1(a) shows model-forecast performance using the log-odds ratio with error bars (Stephenson, 2000) as a function of threshold for the entire time series, and (b) shows the same in terms of the equitable threat score (ETS). The monthly time series of the log-odds ratio at 0.2 mm and 12 mm are shown in Fig. 2(a) and (b). Although the time series are still too short to identify trends it clearly shows the variation in skill at intra-seasonal, seasonal and inter-seasonal time scales.

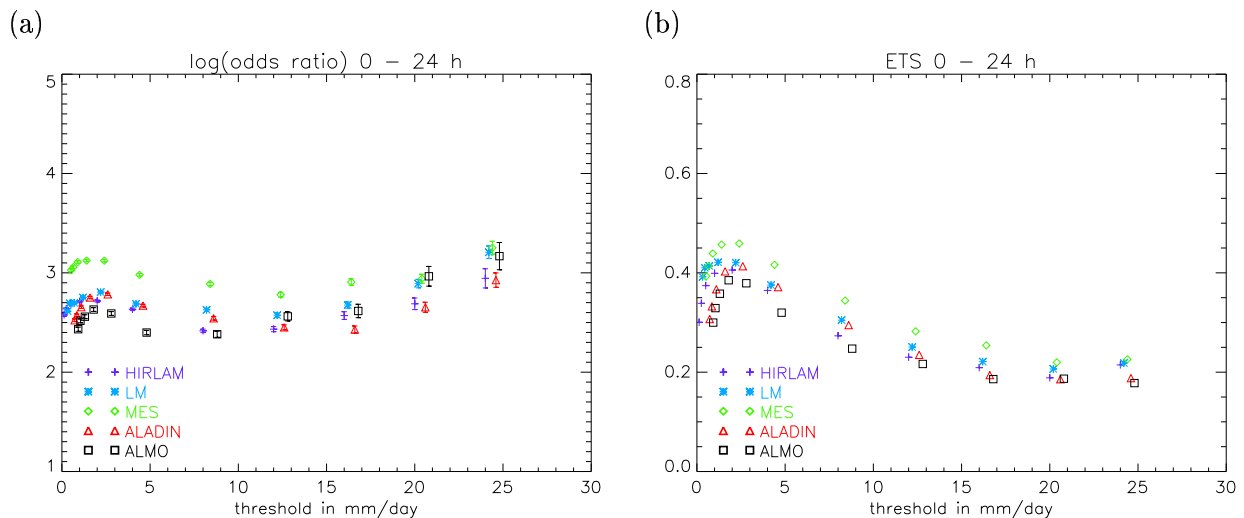


Figure 1: Scores as a function of threshold: (a) log-odds ratio and (b) equitable threat score (ETS) for the period January 2004 to June 2005.

Heavy rainfall between 6–8 January 2005 resulted in accumulations between 40 and 150 mm which led to flooding in north-western England (Carlisle). Figure 3 shows the daily accumulations from various European models (to indicate the coverage) along with the radar accumulation. On the 7th the dry conditions in the south-east are only captured by the UM and the ALADIN. The others show signs of showery outbreaks (aLMo) or more uniform rain. Orographic enhancement is over-estimated by the LM, aLMo and ALADIN (grey areas with > 128 mm).

Acknowledgements Thank you to Meteo France, MeteoSwiss, DWD and FMI for supplying their precipitation forecasts.

*©British Crown Copyright; e-mail:marion.mittermaier@metoffice.gov.uk

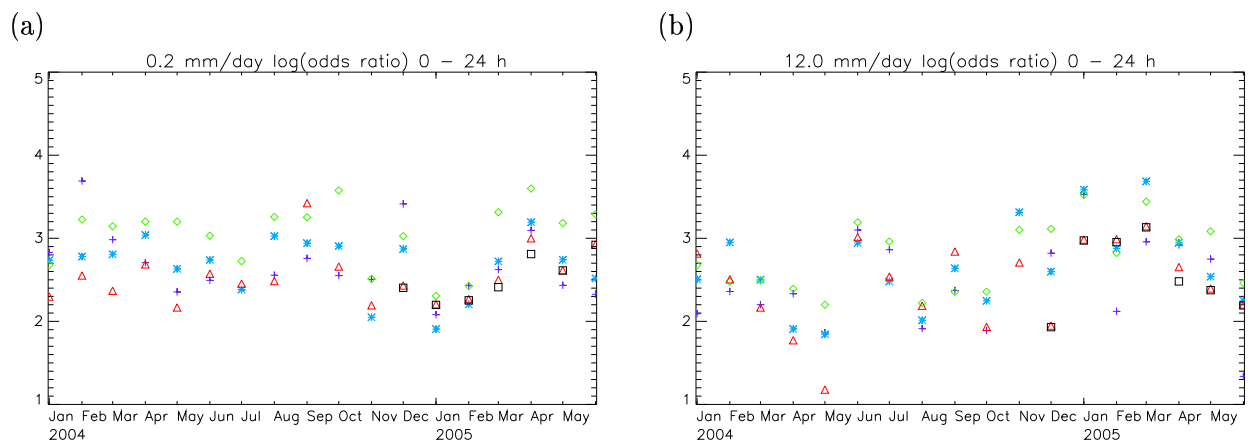


Figure 2: The time series of monthly log-odds ratios: (a) 0.2 mm and (b) 12 mm.

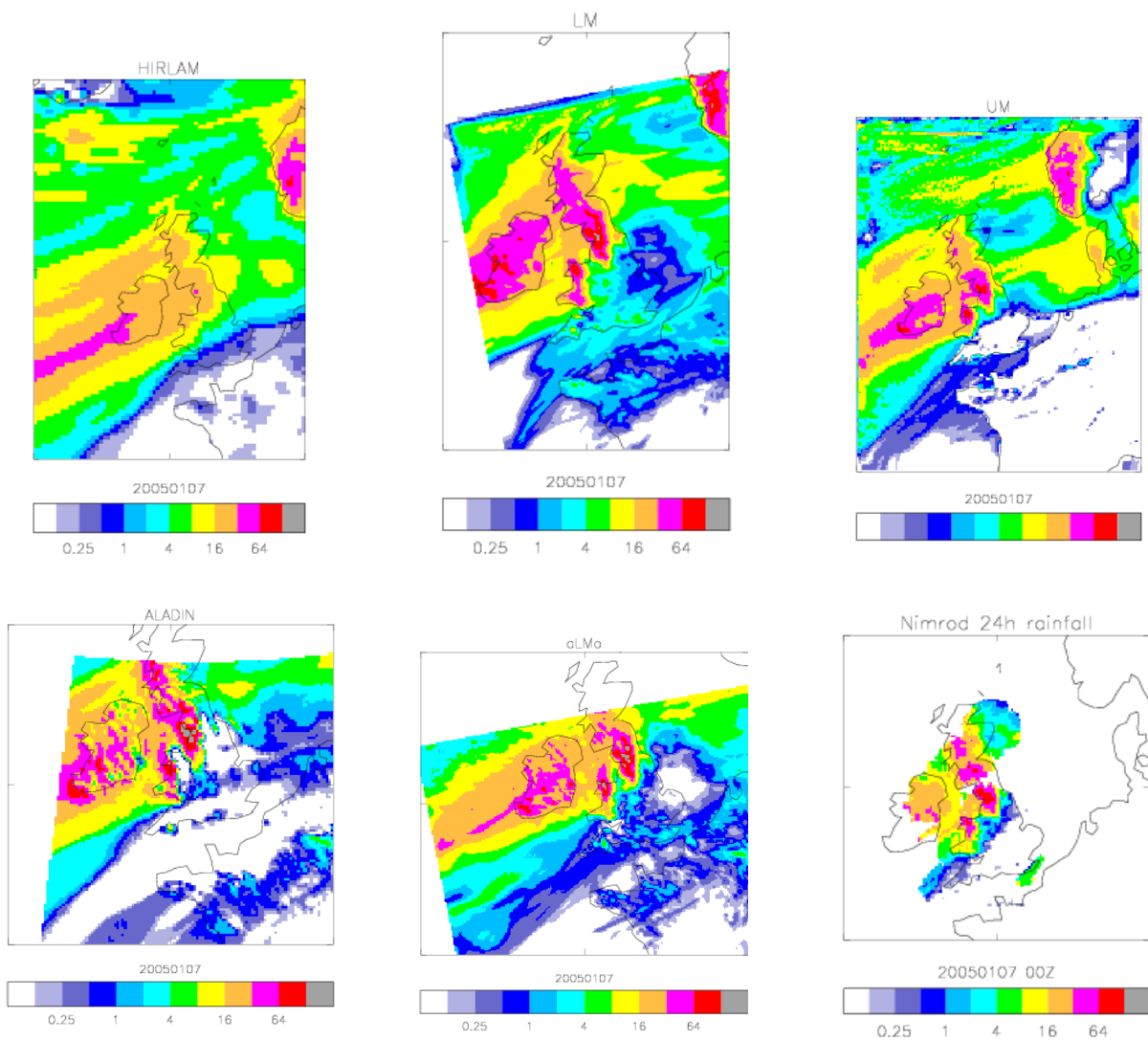


Figure 3: Twenty-four hour accumulations from five European limited-area models for 7 January 2005 along with the verifying radar accumulation.

References

Stephenson, D. B. (2000). Use of the "odds ratio" for diagnosing forecast skill. *Weather and Forecasting*, **15**, 221–232.

**Action as an integral characteristic for climatic structures:
Estimates for atmospheric blockings**

I.I. Mokhov

A.M. Obukhov Institute of Atmospheric Physics RAS, Moscow, Russia
mokhov@ifaran.ru

Analysis has been performed for the atmospheric blockings action S as an integral characteristic of their effect. This value has a dimension [energy]x[time]. Similar characteristic (defined by the integration in time of Lagrange function) is used in theoretical physics (Landau and Lifshits, 2004). First estimates of integral action for atmospheric blockings were cited in the author's presentation at the Institute of Numerical Mathematics RAS in 1997 (see also (Mokhov, 1999; Mokhov, 2006)).

Action S of individual climate structure, in particular for cyclonic or anticyclonic vortices, can be defined as follows

$$S \sim \int I(t) \cdot L^2(t) dt,$$

where integration on time t is performed from 0 to τ , τ – vortex life time, I – vortex intensity (determined by the pressure difference between the vortex centre and periphery, L – vortex size (L^2 characterizes vortex area)).

Integral action S_{Σ} for ensemble of N vortices is defined by the sum of values of action for individual vortices

$$S_{\Sigma} \sim \Sigma \int I(t) \cdot L^2(t) dt.$$

Integral action S_{Σ} can be estimated with the use of mean values for vortex intensity (I_a) and area (L_a^2)

$$S_{\Sigma} \sim N I_a \cdot L_a^2 \cdot \tau.$$

Here the integral action is estimated for blockings using the data for blockings characteristics from (Lupo and Smith, 1995; MAGC, 1997; Wiedenmann et al., 2002) and also from model simulations with different CO₂ content in the atmosphere (Lupo et al., 1997).

Table 1 shows estimates of action for blockings in the Northern Hemisphere: upper line - by data from (Lupo and Smith, 1995); middle line - by data from RIHMI (MAGC, 1997); lower line - by data from (Wiedenmann et al., 2002). Regional and seasonal values $S_{r,s}$ are normalized on the annual hemispheric action $S_{h,a}$. Two variants were used for estimates of blockings action by data from (MAGC, 1997) and (Wiedenmann et al., 2002): with blocking intensity proportional to its size or area.

According to Table 1 the largest contribution to the hemispheric annual action $S_{a,h}$ (characterized by $S_{r,s}/S_{h,a}$) is related with winter blockings (39-54%). At that the basic regional contribution is related with blockings in the Atlantic sector (80°W-40°E): 23-33% during the winter and 55-60% during the year.

The introduction of action allows to estimate total effects of blockings and their changes while tendencies of change for individual characteristics for blockings can be of different sign. Action as an integral characteristic can be also applied for analysis of different atmospheric and oceanic structures and for diagnostics of climatic mechanisms (Mokhov, 2006).

This study was supported by the RFBR and RAS program.

References

Landau, L.D., and E.M. Lifshits, 2004: Theoretical Physics. V.I. Mechanics. Fizmatlit, Moscow, 224 p.

Lupo, A.R., R.J. Oglesby, and I.I. Mokhov, 1997: Climatological features of blocking anticyclones: A study of Northern Hemisphere CCM1 model blocking events in present-day and double CO₂ concentration atmospheres. *Clim. Dyn.*, **13**, 181-195.

Lupo, A.R., and P.J. Smith, 1995: Climatological features of blocking anticyclones in the Northern Hemisphere. *Tellus*, **47A**, 439 – 456.

MAGC, 1997: Monitoring of Atmospheric General Circulation. Northern Hemisphere. Bulletin (1991-1995). RHMC/RIHMI-WDC, Obninsk, 134 pp. (in Russian)

Mokhov, I.I., 1999: Blocking activity in Northern Hemisphere: Detection of change and attribution of causes. Proc. 4th Intern. Conf. on Modelling of Global Climate Change and Variability, MPI, Hamburg, 223.

Mokhov, I.I., 2006: Action as an integral characteristic for climatic structures: Estimates for atmospheric blockings. *Doklady Earth Sci.* (in press)

Mokhov, I.I., and E.A. Tikhonova, 2000: Atmospheric blocking characteristics in the Northern Hemisphere: Diagnostics of changes. Research Activities in Atmospheric and Oceanic Modeling, Ed. By H. Ritchie, WMO TD-No.987, 2.20-2.21.

Wiedenmann, J.M., A.R. Lupo, I.I. Mokhov, and E.A. Tikhonova, 2002: The climatology of blocking anticyclones for the Northern and Southern Hemispheres: Block intensity as a diagnostic. *J. Climate*, **15**, 3459-3473.

Region	Summer VII-IX	Fall X-XII	Winter I-III	Spring IV-VI	Total I-XII
Atlantic (80°W-40°E)	0.01	0.13	0.27	0.15	0.57
	0.06-0.08	0.15	0.23-0.27	0.08-0.09	0.55
	0.02-0.04	0.18-0.20	0.28-0.33	0.05-0.08	0.58-0.60
Pacific (140°E- 100°W)	0.04	0.04	0.09	0.01	0.17
	0.01-0.02	0.05-0.06	0.07-0.08	0.03	0.18
	0.01-0.02	0.06	0.15-0.17	0.03-0.04	0.27
Continental (40-140°E, 100-80°W)	0.02	0.10	0.07	0.07	0.26
	0.02-0.03	0.07-0.08	0.08-0.10	0.07-0.08	0.26-0.27
	0.02-0.03	0.03-0.04	0.04	0.03-0.04	0.12-0.15
Northern Hemisphere	0.07	0.27	0.42	0.23	1.00
	0.10-0.13	0.27-0.28	0.39-0.45	0.18-0.20	1.00
	0.05-0.09	0.28-0.29	0.47-0.54	0.12-0.17	1.00

Table 1. Estimates of action for blockings in the Northern Hemisphere: upper line - by data from (Lupo and Smith, 1995); middle line - by data from RIHMI (MAGC, 1997); lower line - by data from (Wiedenmann et al., 2002). Regional and seasonal values $S_{r,s}$ were normalized on the annual hemispheric action $S_{a,h}$.

Polar Lows as a cyclogeostrophic vortices

I.I. Mokhov

A.M. Obukhov Institute of Atmospheric Physics RAS, Moscow, Russia
mokhov@ifaran.ru

Relative contribution of relative role of cyclostrophic and geostrophic components for intense polar mesocyclones or Polar Lows is estimated with the use data from (Aakjaer, 1992).

In contrast to geostrophic regime with the balance of pressure gradient ($\rho^{-1}(\partial P/\partial r)$) and Coriolis force (fV) the centrifugal force (V^2/r) is significant in the gradient wind equation

$$V^2/r + fV = \rho^{-1}(\partial P/\partial r),$$

for Polar Lows. Here: $f=2\omega \sin\varphi$ – Coriolis parameter, ω - Earth rotation frequency, φ – latitude, ρ – density, V – velocity, P – pressure, r – radius of curvature.

For geostrophic vortices it follows from the equation

$$fV = \rho^{-1}(\partial P/\partial r)$$

that the pressure difference ΔP_c between the periphery and centre of cyclone is proportional to characteristic cyclone velocity V_c and radius r_c

$$\rho^{-1}\Delta P_c \sim f V_c r_c.$$

This regime is characterized by $Ro = V_c/(fr_c) \ll 1$.

Other asymptotic regime ($Ro = V_c/(fr_c) \gg 1$) for cyclostrophic vortices is characterized by the equation

$$V^2/r = \rho^{-1}(\partial P/\partial r)$$

with

$$\rho^{-1}\Delta P_c \sim V_c^2.$$

For intermediate regime with comparable Coriolis and centrifugal forces

$$V^2/r \sim fV,$$

we have

$$Ro = V_c/(fr_c) \sim 1.$$

In this case for polar latitudes with $\sin\varphi \sim 1$ the characteristic cyclone radius r_c is of the order of $V_c/2\omega$. Such vortices for intermediate regime between geostrophic and cyclostrophic ones can be defined as cyclogeostrophic vortices.

Relative role of cyclostrophic and geostrophic components for Polar Lows is characterized by $Ro \sim T_o/(2T_c)$, where $T_c = 2\pi r_c/V_c$ and $T_o = 2\pi/\omega$. Figure 1 shows dependences of Ro on diameter $2r_c$ and intensity ΔP_c for Polar Lows from (Aakjaer, 1992). According to Fig. 1 Polar Lows are cyclogeostrophic vortices with $Ro \sim 1$. Values of T_c are in the range from about $T_o/4 = 6$ hours (for small and less intensive Polar Lows) to about $T_o = 24$ hours (for large and most intensive ones).

This work has been supported by the Russian Foundation for Basic Research and RAS program.

References

Aakjaer, P.D., 1992: *Tellus*, **44A**, 155.

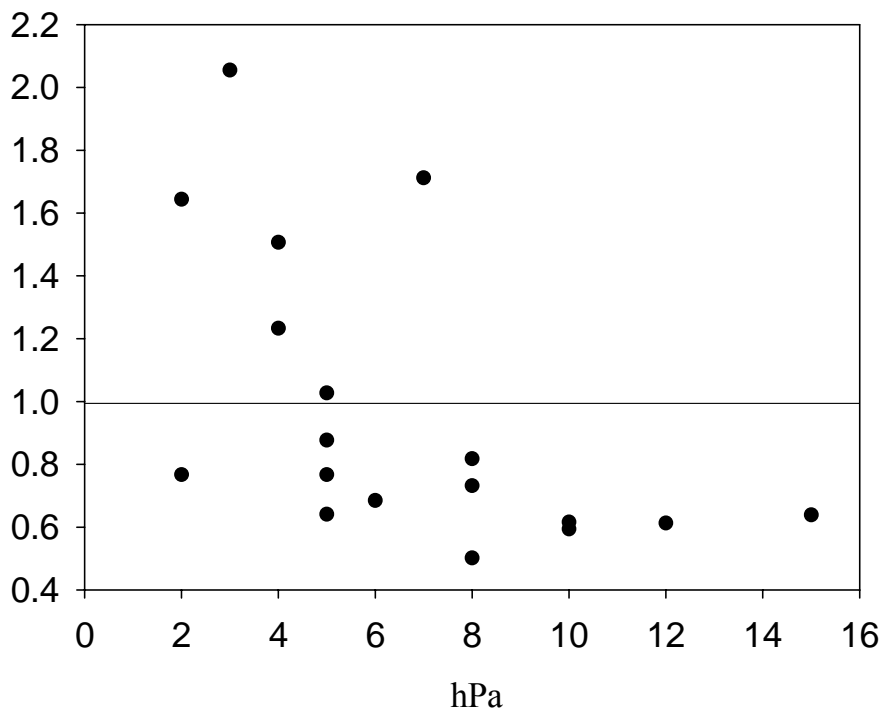
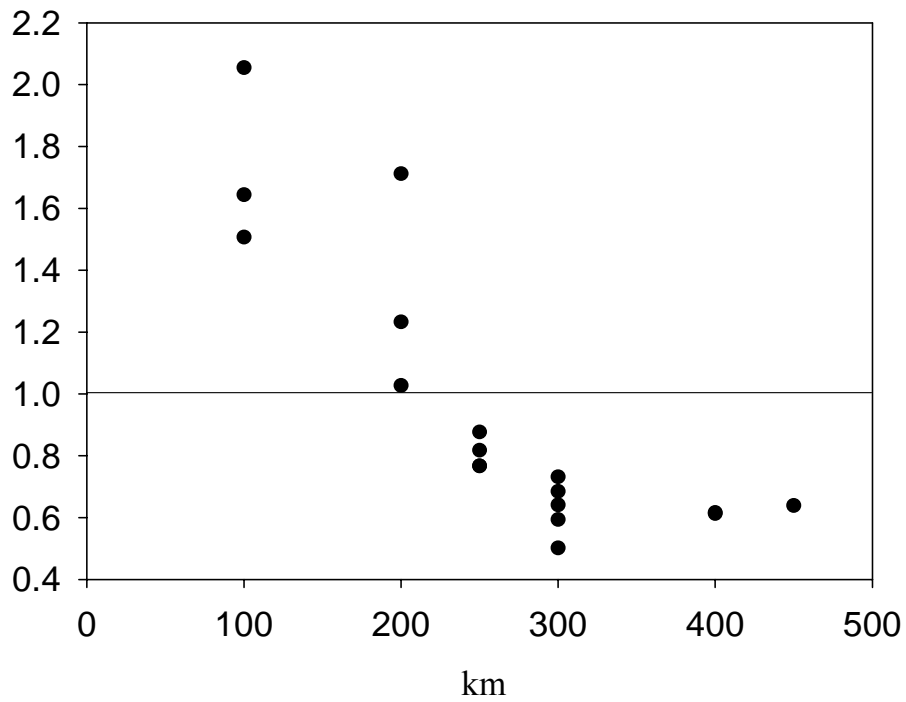


Figure 1. Dependences of Ro on diameter $2r_c$ (km) and intensity ΔP (hPa) for Polar Lows by data from (Aakjaer, 1992).

Relationship between temperature changes near surface in the Arctic and in different regions of the Northern Hemisphere from reanalyses data

Igor I. Mokhov, Andrey A. Karpenko

A.M. Obukhov Institute of Atmospheric Physics RAS, Moscow, Russia
mokhov@ifaran.ru

Assessment of relationship between surface air temperature (SAT) changes in the Arctic as a whole and in different regions of the Northern Hemisphere (NH) has been performed based on data from reanalyses NCEP/NCAR (1948-2001) (Kistler et al., 2001) and ERA40 (1958-2001) (Simmons and Gibson, 2000).

It was noted that the general Arctic warming is accompanied in winter by the SAT decrease over western and northern parts of Atlantic and Pacific Oceans and also over eastern parts of Eurasia and North America (Fig.1). Opposite sign SAT changes are displayed at the same time over eastern and southern parts of oceans and also over western parts of continents.

The displayed dipole regimes over oceans differ from the COWL (Cold Ocean – Warm Land) regimes noted in (Wallace et al., 1995). It is because anomalies in extratropics are not necessary related with an appropriate anomalies in high latitudes. Also the contribution of polar anomalies to the total extratropical anomalies is decreasing due to relatively small area of the Arctic latitudes.

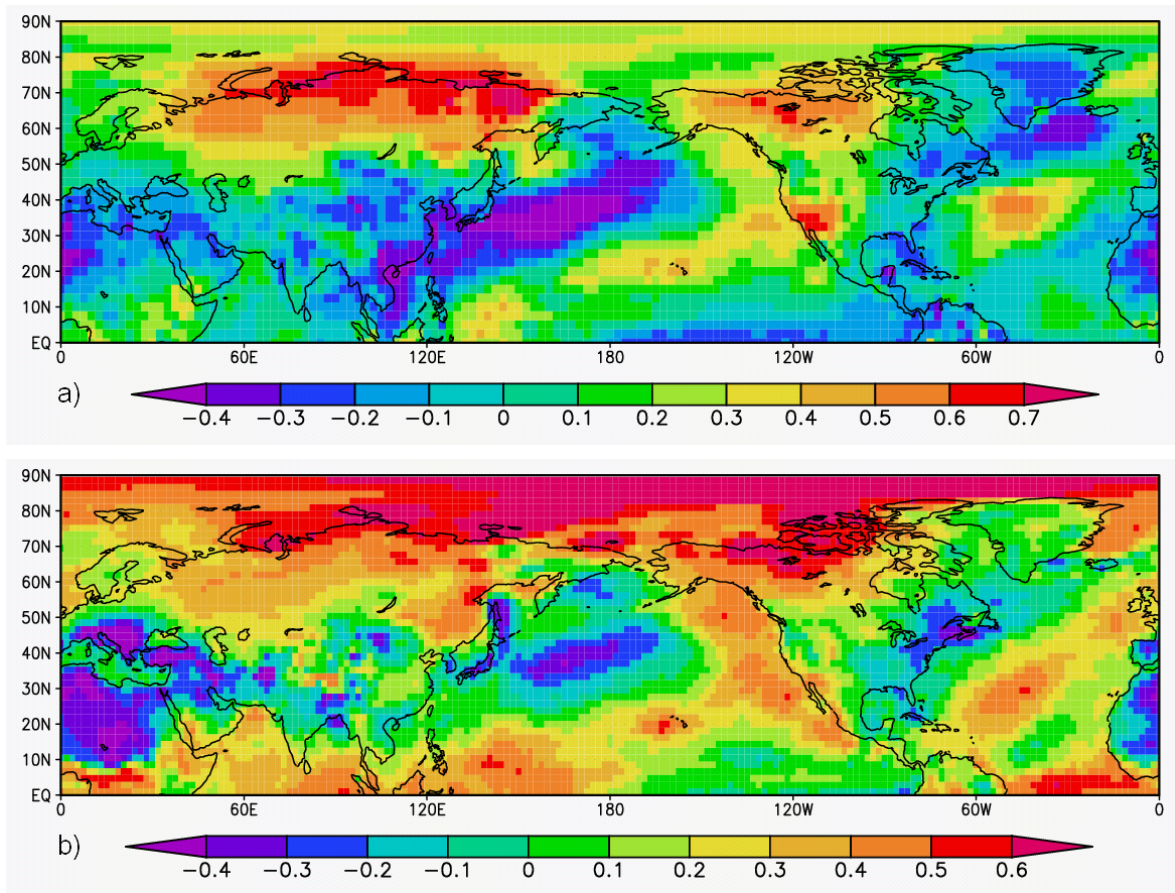
The noted spatial features of a dipole type correspond to the weakening of anticyclonic gyres in the Atlantic and Pacific with a weakening of warm oceanic currents (Gulf Stream and Kuroshio) in western parts of oceans during the Arctic warming.

We thank G.V. Alekseev and R. Barry for useful discussions. This study was supported by the RFBR and RAS program.

References

- Kistler R. et al. The NCEP/NCAR 50-Year Reanalysis: Monthly Means CD-ROM and Documentation. Bull. Amer. Met. Soc. 2001. V.82. P.247-266.
- Simmons A.J., Gibson J.K. The ERA-40 Project Plan. ERA-40 Project Rep. Ser. No.1. ECMWF, Shinfield Park, Reading, UK. 2000. 63 pp.
- Wallace J.M., Zhang Y., Renwick J.A. Dynamic contribution to hemispheric mean temperature trends. Science. 1995. V.270. P.780-783.

Fig.1. Latitude-longitude distribution for coefficients of SAT correlation in the Arctic as a whole (60-90°N) and in different NH regions by reanalyses data for winter seasons: (a) ERA40 (1958-2001), (b) NCEP/NCAR (1948-2001).



Potential fire regimes in regions of Northern Eurasia from meteorological observations and reanalysis

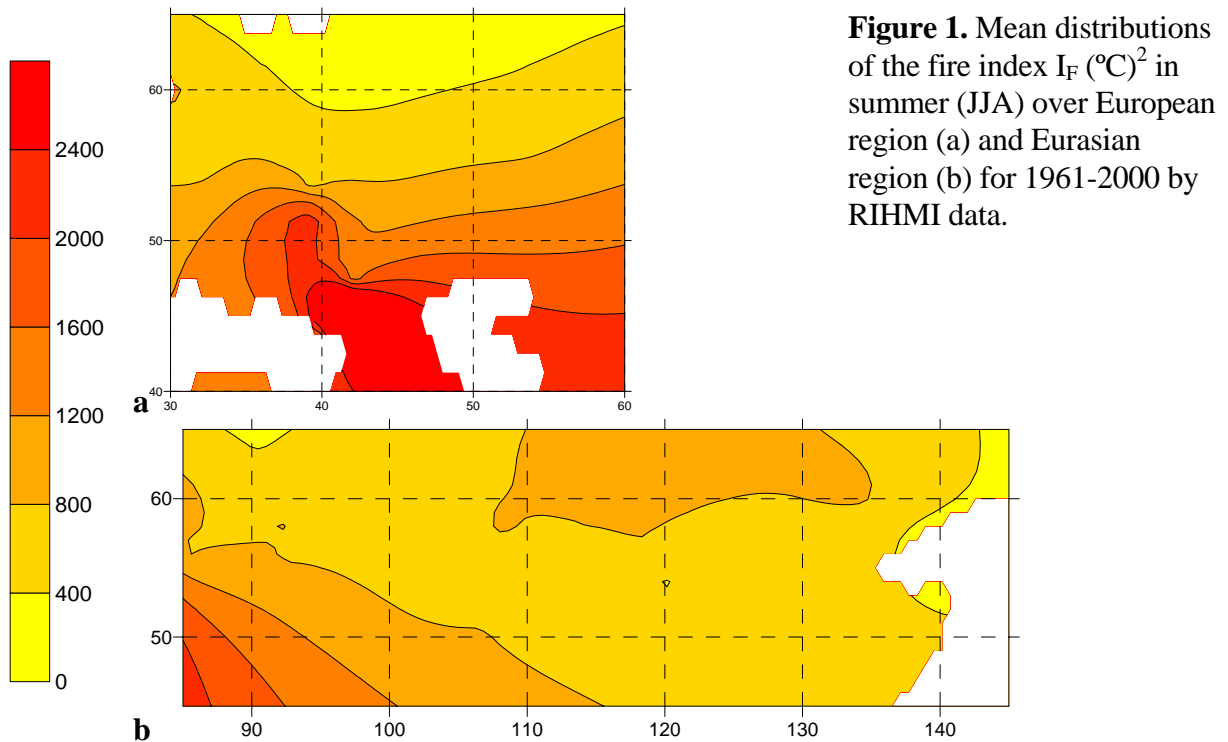
Mokhov I.I., Chernokulsky A.V.

A.M. Obukhov Institute of Atmospheric Physics RAS, Moscow, Russia
mokhov@ifaran.ru

Meteorological observations from the RIHMI (<http://www.meteo.ru>) and the ERA-40 reanalysis data (Simmons and Gibson, 2000) are used for diagnosis of the forest fire conditions in regions of Northern Eurasia (Mokhov et al. 2005). We used different modifications of the Nesterov index I_F for combustibility of forest fires (Nesterov, 1949; Venevsky et al., 2002). In particular, this index was calculated by using maximum daily temperature at the surface, dew-point temperature (defined by relative humidity and temperature) and precipitation. The difference between the two temperatures was multiplied by the daily temperature and summed over the number of days since the first day with daily precipitation less than 3 mm. When the daily precipitation exceeds 3 mm, the I_F value is defined as zero.

$$I_F = \sum_{P < 3mm} T_{max} \cdot (T_{max} - T_{dew})$$

The ignition potentials are considered to be moderate, high and extreme ones for I_F values between 300 and 1000, between 1000 and 4000 and above 4000, correspondingly.



Figures 1a,b show two examples of the I_F distributions for European (a) and Asian (b) regions in summer (June-July-August) for the period 1961-2000 based on Krigging gridding

method by using RIHMI data for 47 Russian meteorological stations (17 stations for European part and 30 stations for Asian part) with the most detailed data.

Changes of fire regimes can be characterized by the relation k of I_F to its mean value $\langle I_F \rangle$ for the control period 1961-1990. According to observations values of $\langle I_F \rangle$ equal to $1605 \text{ (}^\circ\text{C)}^2$ for Moscow and $1568 \text{ (}^\circ\text{C)}^2$ for Irkutsk. For estimates from reanalysis data we used surface air temperature at noon T_{12h} instead of T_{max} . According to reanalysis data values of $\langle I_F \rangle$ equal to $1041 \text{ (}^\circ\text{C)}^2$ for Moscow and $570 \text{ (}^\circ\text{C)}^2$ for Irkutsk.

We also analyzed the probability $P(k>2)$ for exceeding of $k=2$. Figure 2 display changes of $P(k>2)$ in summer for Moscow in European region (a) and for Irkutsk in Asian region (b) from observations (RIHMI) and reanalysis data (ERA-40). In particular, the largest values of $P(k>2)$ for Moscow in summer were noted in 1972 and 2002.

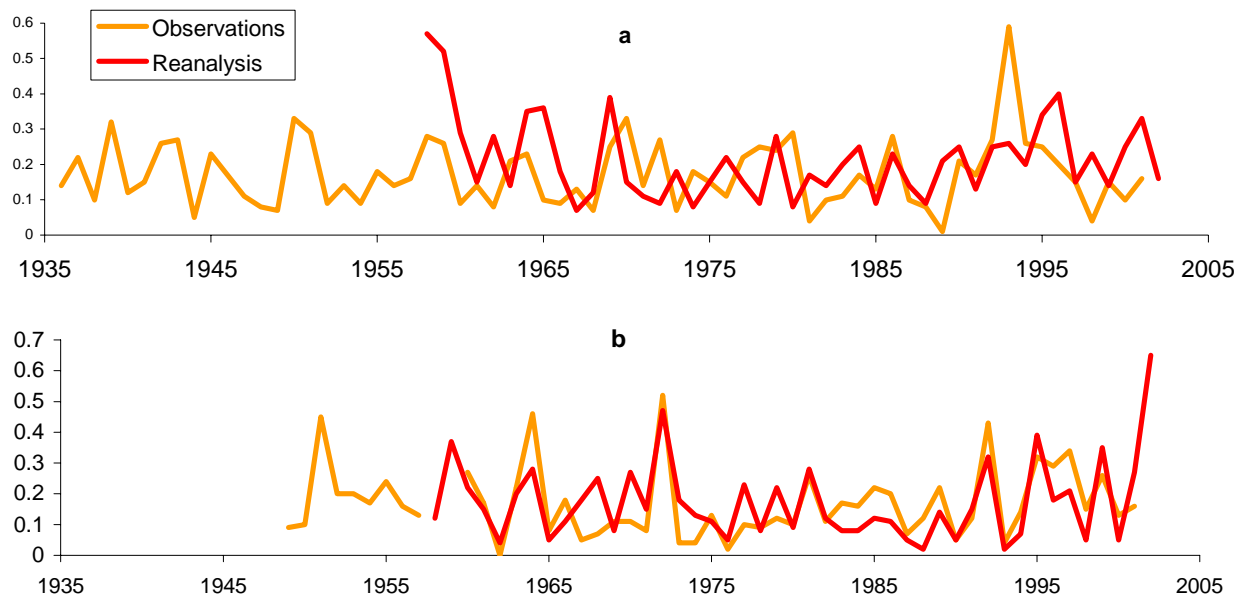


Figure 2. Changes of $P(k>2)$ in summer for Moscow (a) and for Irkutsk (b) from observations and reanalysis data.

We thank V.N. Razuvayev for his help to get daily meteorological data from the RIHMI. This study was supported by the RFBR and RAS program.

References

- Mokhov, I.I., A.V. Chernokulsky, V.Ch. Khon, and V.A. Tikhonov, 2005: Regional Changes of extreme dry conditions from observations and reanalysis for regions of Northern Eurasia. EGU General Assembly 2005, Geophysical Research Abstracts, **7**.
- Nesterov, V.G., 1949: Gorimost' lesa i metody ee opredeleniya. Goslesbumaga. Moscow. 74 pp. (In Russian)
- RIHMI: <http://www.meteo.ru>
- Simmons, A.J., and J.K. Gibson, 2000: The ERA-40 Project Plan, ERA-40 Project Report Series No. 1, ECMWF, Shinfield Park, Reading, UK. 63 pp
- Venevsky, S., K. Thonicke, S. Sitch, and W. Cramer, 2002: Simulating fire regimes in human-dominated ecosystems: Iberian Peninsula case study. *Global Change Biology*, **8**, 984-998.

Generating Regional High-Resolution Air Temperature Fields Using MODIS LST Data

Georgy V. Mostovoy, K. Raja Reddy and Roger L. King
Mississippi State University, Mississippi State, MS 39762, USA
E-mail: mostovoi@gri.msstate.edu

The land skin/surface temperature (LST) retrieved from the Moderate Resolution Imaging Spectro-Radiometer (MODIS) TIR measurements (MODIS, 2001) with nominal accuracy of 1°C can be used successfully for linear regression estimates of daily air maximum and minimum temperatures at a regional scale (Kawashima et al., 2000; Jones et al., 2004; Mostovoy et al., 2006). MODIS LSTs have the relatively high spatial resolution of 1km and 5 km, revisiting frequency (twice a day), and global coverage. Previous studies (Florio et al., 2004) demonstrated that use of satellite-derived LST as an additional covariate resulted in an improvement of air temperature spatial interpolation quality over the areas not covered with meteorological observations.

Both *in situ* surface observations of the air temperature from 161 stations and MODIS LST data were selected for the period from June 2000 to the end of 2004. Two groups of MODIS LST products were used. They were available globally at approximately 10:30 AM/PM (*Terra* platform) and 1:30 AM/PM (*Aqua* platform) local solar time. This study was performed over the regular domain having extension of 4.0° in longitude and 5.5° in latitude, encompassing the entire state of Mississippi (Fig. 1).

Spatial interpolation accuracy of air temperature (both daily maximum and minimum) fields has been evaluated in terms of mae (mean absolute error), root-mean-square error (rmse), and bias (mean difference between interpolated and observed values). 18 sites evenly distributed over the state of Mississippi have been eliminated from interpolation procedures and used for accuracy evaluation (Fig. 1 shows the sites locations). The interpolation procedure utilizes thin-plate splines for spatial representation of air temperature and LST fields and has been performed in two basic versions: without (control case) and with MODIS 5-km LST data (LST case). Distribution of the interpolation errors showed marked spatial (Fig. 1) and seasonal features (Fig. 2) over the state of Mississippi with a distinct minimum of mae and rmse values during July-Aug. period and higher values of errors exceeding 2°C at winter months. Dashed lines in Fig. 2 stand for the control case and solid for the LST case. Fig. 2 provides a clear evidence that inclusion of MODIS 5-km LST data into interpolation scheme results in a persistent improvement of air temperature interpolation accuracy (both for daily maximum and minimum) seen as a reduction of mae and rmse values.

Seasonal weather variability and surface cover parameters have proven to be the most important factors controlling observed spatial and temporal variations of the interpolation errors (Mostovoy et al., 2006).

References

- Florio, E.N., Lele, S.R., Chi Chang, Y., Sterner, R. and G.E. Glass, 2004, "Integrating AVHRR satellite data and NOAA ground observations to predict surface air temperature: a statistical approach," *International Journal of Remote Sensing*, 25: 2979-2994.
- Jones, P., G., Jedlovec, R., Suggs and S. Haines, 2004, "Using MODIS LST to estimate minimum air temperatures at night," in *13th Conference on Satellite Meteorology and Oceanography* (preprints), Norfolk, VA: AMS, 4.13 (CD-ROM).
- Kawashima, S., T., Ishida, M., Minomura and T. Miwa, 2000, "Relations between surface temperature and air temperature on a local scale during winter nights," *Journal of Applied Meteorology*, 39: 1570-1579.
- MODIS Data Products, 2001, Land Processes Distributed Active Archive Center. [<http://edcdaac.usgs.gov/modis/dataproducts.asp>].
- Mostovoy, G.V., King, R.L., Reddy, K.R., Kakani, V.G. and M.G. Filippova, 2006, "Statistical estimation of daily maximum and minimum air temperatures from MODIS LST data over the state of Mississippi," *GIScience and Remote Sensing*, 43: 62-94.

Frontal identification in digital analyses

Hilary Newstead and Ian Simmonds

School of Earth Sciences
The University of Melbourne
Victoria, 3010, Australia

We report on our plans and progress to develop a sophisticated, objective frontal identification and tracking algorithm able to be applied to reanalyses or model output. This problem has attracted only modest amounts of attention over recent decades. However, there have been significant landmarks in its development, and among these may be mentioned the works of Renard and Clarke (1965), Huber-Pock and Kress (1989), Huth (1991), Hewson (1998), McCann and Whistler (2001) and Kašpar (2003). The scheme we are developing is designed to make optimum use of information on the three dimensional structure of the thermal, moisture and dynamic fields. A particular focus of our work is on frontal systems in the Southern Hemisphere.

The approach to the automatic identification of fronts depends considerably on the spatial resolution available. SeaWinds-on-QuikSCAT scatterometer surface winds provides resolution of 25 km, and Patoux et al. (2005) have shown this data is capable of providing extraordinary detail for fronts over the Southern Ocean. One limitation of using such data is that only the surface manifestation of frontal systems can be explored, and use can only be made of the dynamical (*viz* the wind) structures at that level. Our aim is to use numerous variables in three dimensions, and hence part of our work is devoted to exploring frontal structures in high resolution models. We are making use of the output of the Australian 'ALAPS' model (Adams, 2004). Figure 1 shows a very preliminary version of the frontal identification scheme applied to the surface wind field of an arbitrarily chosen (29/12/2000 at 500 UTC) 6-hour forecast of the ALAPS model run at 0.375° lat-long. resolution. Use is now being made of the wind and other variables in the model throughout the troposphere.

In concert with the 'identification' phase are also developing software which will provide the 'optimum' method for tracking fronts. The first approach will be a generalization of the robust scheme we have already developed for cyclone centres (Simmonds and Keay, 2000; Simmonds et al., 2003).

References

- Adams, N., 2004: A numerical modeling study of the weather in East Antarctica and the surrounding Southern Ocean. *Weather and Forecasting*, **19**, 653-672.
- Hewson, T. D., 1998: Objective fronts. *Meteorological Applications*, **5**, 37-65.
- Huber-Pock, F., and C. Kress, 1989: An operational model of objective frontal analysis based on ECMWF products. *Meteorology and Atmospheric Physics*, **40**, 170-180.

- Huth, R., 1991: An attempt to objectivize the frontal analysis. *Idojaras - Journal of the Hungarian Meteorological Service*, **95**, 1-19.
- Kašpar, M., 2003: Objective frontal analysis techniques applied to extreme/non-extreme precipitation events. *Studia Geophysica Et Geodaetica*, **47**, 605-631.
- McCann, D. W., and J. P. Whistler, 2001: Problems and solutions for drawing fronts objectively. *Meteorological Applications*, **8**, 195-203.
- Patoux, J., G. J. Hakim and R. A. Brown, 2005: Diagnosis of frontal instabilities over the Southern Ocean. *Monthly Weather Review*, **133**, 863-875.
- Renard, R. J., and L. C. Clarke, 1965: Experiments in numerical objective frontal analysis. *Monthly Weather Review*, **93**, 547-556.
- Simmonds, I., and K. Keay, 2000: Mean Southern Hemisphere extratropical cyclone behavior in the 40-year NCEP-NCAR reanalysis. *Journal of Climate*, **13**, 873-885.
- Simmonds, I., K. Keay and E.-P. Lim, 2003: Synoptic activity in the seas around Antarctica. *Monthly Weather Review*, **131**, 272-288.

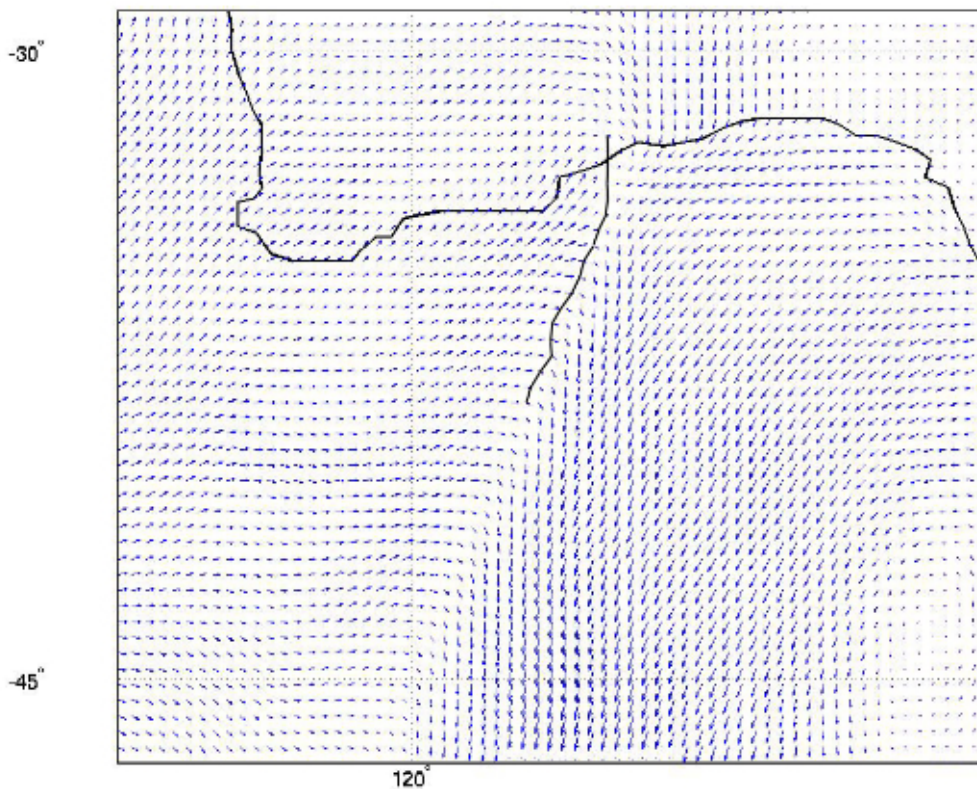


Figure 1: An example of a very preliminary version of the frontal identification scheme applied to the surface wind field of an arbitrarily chosen (29/12/2000 at 500 UTC) 6-hour forecast of the ALAPS model (Adams, 2004) run at 0.375° lat-long. resolution.

ISOTOPIC COMPOSITION OF WATER VAPOR MODELED BY CONSTRAINING GLOBAL CLIMATE SIMULATIONS WITH REANALYSES

David Noone (dcn@colorado.edu)

Department of Atmospheric and Oceanic Sciences, and Cooperative Institute for Research in Environmental Sciences, University of Colorado, Boulder, CO, USA

Simulations of the stable isotope composition (ratio of HDO or H₂¹⁸O to H₂O) of water reservoirs and fluxes in climate models can be used to help diagnose which aspects of the model hydrologic cycle and clouds are accurately represented, and which are not. Early global isotope models used bulk exchange schemes to represent the isotopic changes during condensation and evaporation, which was of a similar level of complexity to the underlying cloud parameterizations (e.g., Noone and Simmonds, 2002). With the advent of more elaborate cloud schemes and the inclusion of multiple water phases, a new strategy for simulating isotopes that is of comparable complexity is required. Such a scheme has been added to the NCAR Community Atmosphere Model Version 3. Nonetheless, simulated isotopic distributions from climate models, although credible, can be compared with observations (from satellite, aircraft and surface sampling) only in a statistical manner since the model's atmospheric circulation does not match the observed, and thereby their practical use is limited. Specifically, diagnosing shortcomings in cloud parameterizations with isotopes is presently confounded by the lack of sufficient observational data for meaningful statistical comparison, while data is available for case studies.

To simulate isotopic composition that matches the synoptic conditions, a scheme is developed by which the atmospheric circulation is constrained by reanalysis data, while the hydrology is free to evolve as governed by the model's parameterizations. The constrained simulation proceeds as follows: 1) A global prediction is made for $\Delta t=6$ hours, when reanalysis data is next available; and 2) the predicted horizontal velocity and temperature are corrected by relaxing to the Reanalysis with an adjustment of the form

$$\hat{T} = T + \eta \frac{\Delta t}{\tau} (T_{NCEP} - T)$$

and similarly for u and v wind components. The relaxation time scale is set uniformly as $\tau = 24$ hours, which is typical for adjustment to geostrophic flow in midlatitudes. The factor η varies vertically from unity above $\sigma=0.850$, and reduces linearly to zero at and below $\sigma=0.950$, such that there is no adjustment performed near the surface - the rationale being that boundary layer conditions are strongly dependent on the specific physical parameterizations. The 6 hour predictions and corrections are continued until a simulation of desired length is achieved. In practice it is convenient to configure CAM to use the same 28 σ levels as the NCEP Reanalysis, while the NCEP Reanalysis is first truncated to T42 spherical harmonic resolution, and the topography from the NCEP Reanalysis is used to minimize possible mismatch. Although this simple scheme conserves neither momentum nor energy, the results are remarkably satisfying, largely because the 6 hour forecasts are reasonably accurate. Figure 1a shows that differences in surface pressure between 6 hour predictions and Reanalysis is typically less than 1 hPa. Given

the horizontal resolution, the predicted water vapor fields match the Reanalysis well in the midlatitudes, while in the tropics greater difference is attributed to the stronger dependence on the details of the cloud parameterization (Fig. 1b). Further, a limitation of this scheme is that by adjusting the temperature, there is a thermodynamic inconsistency between the water vapor and temperature fields, which can lead to spurious condensation events in the tropics. This is partially due to the selection of a uniform τ based on midlatitude considerations. One strength of the scheme is that both total mass and water vapor mass are conserved, which is necessary for accurate isotope simulations. Successful isotopic simulations are evidence that the dynamically constrained hydrology is performing well (Fig. 1c). Indeed, since the water vapor and isotopic fields are not adjusted, the predicted precipitation fields are free from some of the known biases in the Reanalysis associated with assimilation of radiosonde moisture profiles. As such, the isotopic simulations can be reliably compared to available observations to diagnose which aspects of the model hydrology do not perform as desired.

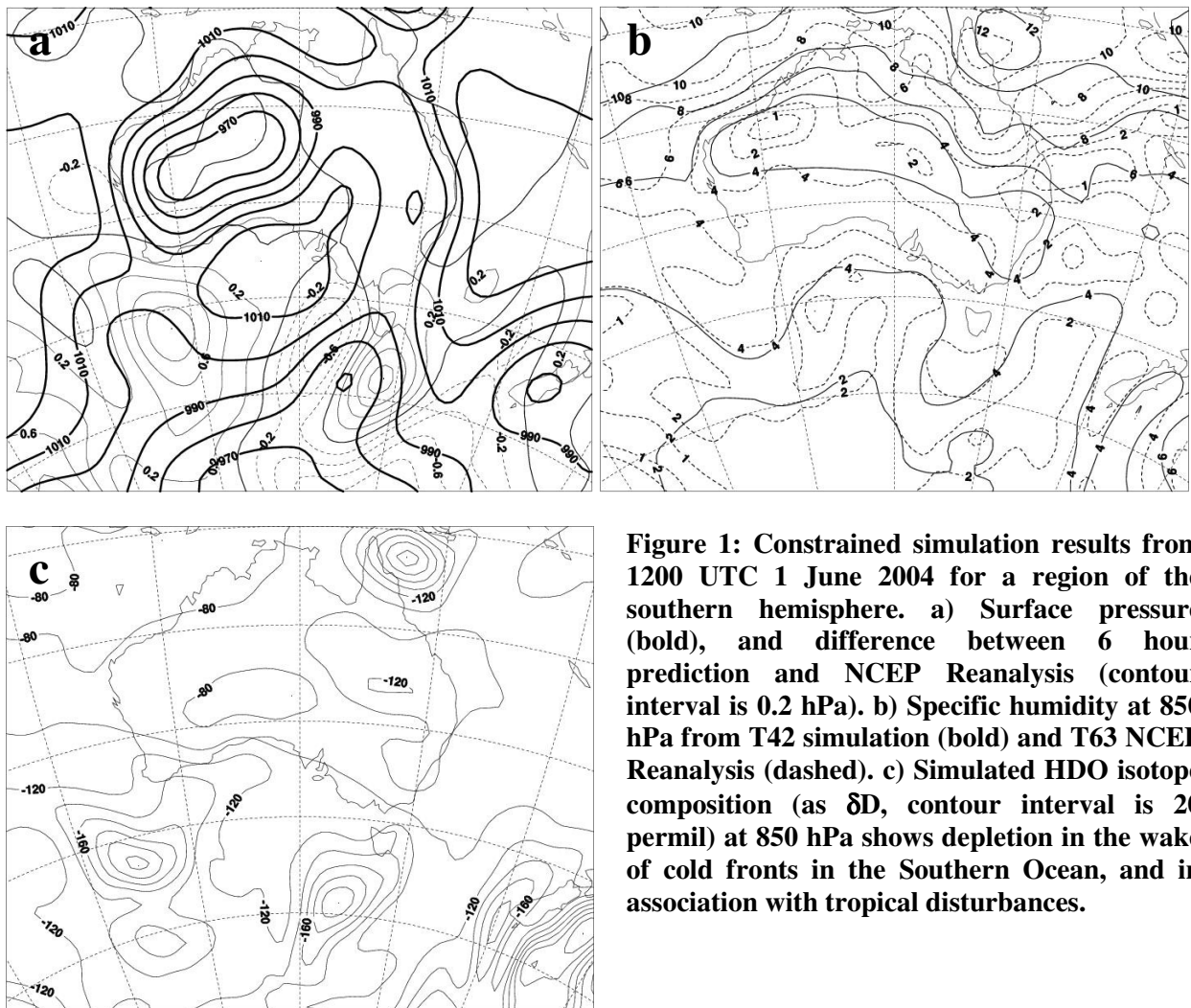


Figure 1: Constrained simulation results from 1200 UTC 1 June 2004 for a region of the southern hemisphere. a) Surface pressure (bold), and difference between 6 hour prediction and NCEP Reanalysis (contour interval is 0.2 hPa). b) Specific humidity at 850 hPa from T42 simulation (bold) and T63 NCEP Reanalysis (dashed). c) Simulated HDO isotope composition (as δD , contour interval is 20 permil) at 850 hPa shows depletion in the wake of cold fronts in the Southern Ocean, and in association with tropical disturbances.

Noone, D., and I. Simmonds, 2002: Associations between $\delta^{18}O$ of water and climate parameters in a simulation of atmospheric circulation for 1979-1995. *Journal of Climate*, **15**(22), 3150-3169.

Influences of the Pacific Decadal Oscillation on the Southern Hemisphere extratropical climate

Alexandre Bernardes Pezza and Ian Simmonds

School of Earth Sciences, The University of Melbourne, Victoria 3010, Australia

e-mail: apezza@unimelb.edu.au

The Southern Hemisphere (SH) climate is strongly associated with variability in the Pacific Ocean. The El Niño has been one of the most studied interannual modes of variability (Karoly 1989), but in the last decade the term Pacific Decadal Oscillation (PDO) was also introduced in connection to a long-lived ENSO-like pattern seen in the lower frequencies (Mantua et al 1997). The PDO is well documented for its impacts particularly over the extratropical Northern Hemisphere (Mantua et al 1997), but very little is known in the case of the SH. A recent assessment on the global rainfall variability at different time scales has stressed its importance at the decadal and interdecadal time scales, with enormous implications for agricultural management (Meinke et al 2005).

We are studying the association between the PDO and the cyclone/anticyclone behavior in the SH through an automatic procedure developed at Melbourne University (Simmonds et al 2003). The tracking scheme calculates each individual synoptic trajectory and summarizes the statistical properties from a climate perspective, either regionally or for the large scale. This technique has been applied in terms of Depth (DP), which is an objective measure of cyclone/anticyclone strength. Composites of this property and Mean Sea Level Pressure were calculated for the years when the PDO index was greater than the average plus one standard deviation (PDO⁺) or lower than the average minus one deviation (PDO⁻), using the ERA 40 reanalysis data set for the period 1958-2002.

The MSLP shows a strong annular structure related to the PDO, with lower pressure around Antarctica when the PDO index is positive, and higher pressure over much of the eastern hemisphere (Figure 1). The DP response presents a coherent pattern indicating greater values when the PDO is positive (Figure 2), indicating that more intense cyclones are found not only over the areas where the pressure is lower, but also spreading out further north around the SH. The DP anomalies are significant when compared to the climatology, and the most intense anomalous regions are statistically significant up to 99% according to the t-student test.

Karoly, DJ, 1989: Southern Hemisphere circulation features associated with El Nino - Southern Oscillation events. *Journal of Climate*, **2**, 1239-1252.

Mantua, N.J., Hare, S.R., Zhang, Y., Wallace, J.M., Francis, R.C., 1997: A Pacific Interdecadal Climate Oscillation with Impacts on Salmon Production. *Bulletin of the Am. Met. Soc.*, **78**, 1069-1079.

Meinke, H, DeVoil, P, Hammer, GL, Power, S, et al., 2005: Rainfall variability at decadal and longer time scales: signal or noise? *Journal of Climate*, **18**, 89-96.

Simmonds, I., Keay, K., Lim, E., 2003: Synoptic Activity in the Seas around Antarctica. *Monthly Weather Review*, **131**, 272-288.

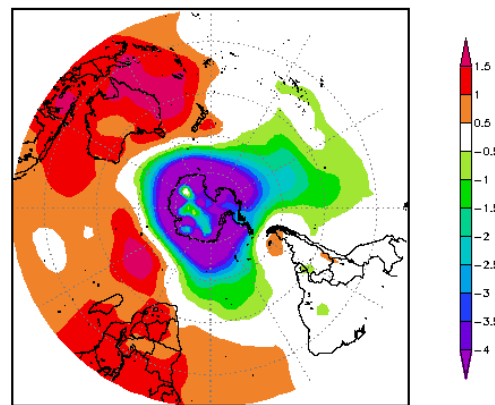


Figure 1: Annual mean sea level pressure anomalies for PDO^+ - PDO^- for the period 1948 – 2004. Total number of years used in the composite: PDO^+ 9 years, PDO^- 15 years.

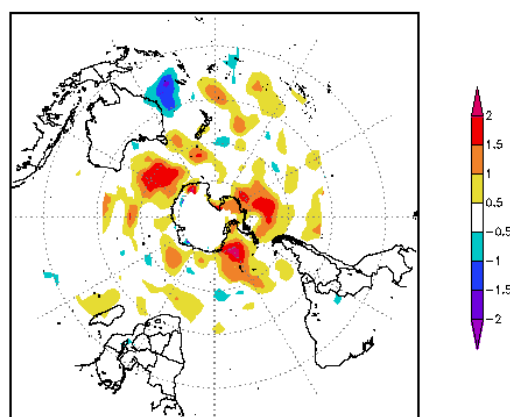


Figure 2: Cyclone Depth for the PDO^+ - PDO^- during the 1958-2002 summer season (DJF). Total number of years used in the composite: PDO^+ 8 years, PDO^- 9 years.

The Relationship between Cyclone Characteristics and Annual Hydrological Resources over Québec

Corina Rosu, Peter Zwack and René Laprise

Department of Atmospheric Sciences, UQAM, Montréal (Québec) Canada

Email: rosu@sca.uqam.ca, laprise.rene@uqam.ca

1. Introduction

Cyclones can be considered as a significant component of the climate, because they are responsible for the most weather variations. They are also the origin of many extreme events. Variations of cyclone tracks have been related to large-scale circulation variability such as NAO and ENSO. In this article we will present the link between cyclone characteristics and the annual hydrological resources for one basin in Québec for the period 1960-1999.

2. Data Set

The diagnostic part of the study is performed using the NCEP 40-yr re-analysis data set (1960-1999) with a horizontal resolution of 2.5° , based on the orography, 1000-hPa geopotential, and 500-hPa wind. We also use the flow of natural water contribution from two hydrological basins of Québec (Outaouais and St-Maurice hereinafter grouped and noted OM).

3. Methodology

In order to find the main characteristics of the temporal and spatial cyclone distribution, we used two algorithms: the first permits to identify the cyclone centers and to organize them in tracks, Sinclair's algorithm (1994, 1997), while the second measures the occurrence, developed by Rosu (2005).

The cyclone tracks have been computed using the technique developed by Murray and Simmonds (1991), Sinclair (1994, 1997) and slightly improved by Rosu (2005). In Sinclair's algorithm, the tracking of the cyclones is undertaken with the 1000-hPa gradient-wind vorticity field, and the maxima are detected by comparing with the eight closest points. These maxima have to be larger than a selected threshold value. The tracking itself is performed at each 6 hours. To define the trajectory of a cyclone requires agreement between three characteristics of the cyclone center at the time t with the same three characteristics of the cyclone center at the next time. Thus, for each cyclone at the time t , a triple prediction is required, concerning the position, pressure and vorticity for the next point of the trajectory. The prediction is based on the history of the movement, pressure value, vorticity tendency and half of the value of the wind at 500hPa (Zwack, personal communication). When an agreement between the prediction and the analyses at the time t is satisfied, we consider that the next point of the trajectory is found.

In order to remove the weak perturbations and quasi-stationary centres, we imposed a set of conditions:

- ξ_g threshold is considered of 2.5×10^{-5} ;
- minimal value of track lifetime is one day;
- minimal track length is 1200 km.

Several statistical measurements were performed using the second part of the software: five density (cyclone density, tracks density, genesis density, lysis density and strong system density), five means (mean velocity, mean circulation, mean lifetime, mean speed and mean precipitable water), and also system density and mean velocity. All the statistics were directly calculated onto a sphere (we did not use projection), on a latitude-longitude grid, with the distance between the grid points of $2.5^\circ \times 2.5^\circ$. In our calculation, we used statistics circles of 3° latitude centered on each grid point. Because the distance between the grid points is about 2.5° latitude and the statistics circle radius is 3° latitude, there is the risk to compute of many times the same cyclone which is located on the common area of the circles which are partial superimposed (for a detailed description of this algorithm, see Rosu 2005).

Because the most significant contribution of yearly water is recorded during the three months of March, April and May, we studied the entire year by taking in account these three months. The contribution of these three months during the 40 years of study was classified according to the standard deviation criteria. Thus, we obtain 12 years of strong hydraulicity (wet period, noted H "humide") and 17 years of weak hydraulicity (dry period, noted S "sec").

The present study shows two cyclone characteristics for seven months (NDJFMAM): cyclone density - the number of all the cyclone centers at the time of the analysis inside the circle of 3° latitude (number/month) - and track density - the number of all the trajectories that pass through the circle of 3° latitude (number/month). Our study was focused to find a relation between the water contribution observed during the three months (MAM) and the characteristics of the cyclones recorded during the period 1960-1999.

4. Results and analyses

Figures 1 and 2 show the Québec geographical distribution of cyclone system density and cyclone track density for 7-month cycle (from November to May) as a function of hydraulicity of two basins. The patterns and values are rather uniform, except over the area at the South-East of the region OM, where more frequent cyclones are present in periods of high hydraulicity.

The distribution of the monthly average of the cyclone number (fig. 3a) shows that there is a larger cyclone number for the wet period than for the dry period over the OM region, during the months MAM.

For the cyclone direction, fig. 3b reveals an increase of 11% during the wet period. Also, one notes significant increases in directions E and SE. Thus, there is an increase of cyclones coming from the Great Lakes and the James Bay during the wet years for the cyclones.

5. Conclusions

For the study period over the OM region, we noted an increase of 20% of the cyclones and trajectories number for the wet period; the maximum of densities are recorded for the areas located over or in the vicinity of the Appalachian Mountains. The position of this maximum and the favoured

displacement of the cyclones towards the North-East result in increased precipitations in the OM region during the wet years

Concerning the cyclone direction for the MAM, a strong increase of the number of cyclones moving towards the East and North-East is noted during the wet period.

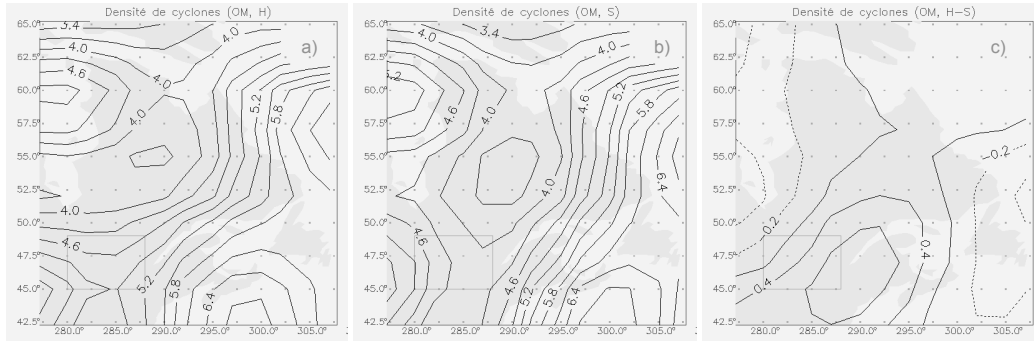


Figure 1: Cyclone system density during period (a) of strong hydraulicity (H), (b) of weak hydraulicity (S) and (c) the difference (solid lines for positive differences and dashed lines for negative differences). Contour interval every 0.2 centers per 3° latitude circle per month.

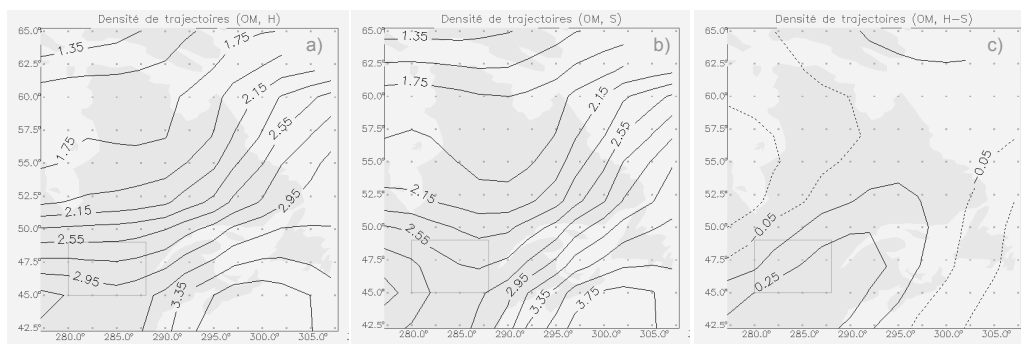


Figure 2: Cyclone track density during period (a) of strong hydraulicity (H), (b) of weak hydraulicity (S) and (c) the difference (solid lines for positive differences and dashed lines for negative differences). Contour interval every 0.15 tracks per 3° latitude circle per month.

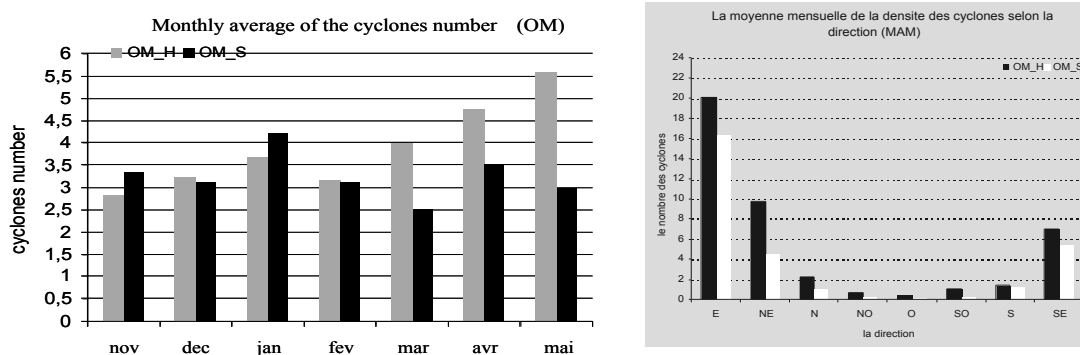


Figure 3: Monthly average of the cyclone number observed about the basins OM during the strong (H) and weak (S) hydraulicity periods (a), and monthly average of the cyclone system density function of cyclone direction (b).

Murray, R. J., and I. Simmonds, 1991a: «A numerical scheme for tracking cyclone centres from digital data. Part I: Development and operation of the scheme». *Aust. Meteor. Mag.* **39**, p. 155–166.

Rosu, C.E., 2005: «Le lien entre les caractéristiques des cyclones et l'hydraulicité au-dessus du Québec», M. Sc. Dissertation, UQÀM.

Sinclair, M. R., 1994: «An objective cyclone climatology for the Southern Hemisphere». *Mon. Wea. Rev.*, **122**, p. 2239–2256.

Sinclair, M. R., 1997: «Objective identification of cyclones and their circulation intensity and climatology». *Wea. Forecasting*, **12**, p. 595–611.

MULTILAYERED PRECEPTRONS FOR PRECIPITATION PREDICTION IN BULGARIA BASED ON NWP MODELS

Ivan Tsonevsky, Valery Spiridonov

National Institute of Meteorology and Hydrology, 66 Tzarigradsko Chaussee, 1784
Sofia, Bulgaria

e-mail: Ivan.Tzonevski@meteo.bg

Neural networks are used for modelling of complex, non-linear dynamical phenomena. They have a wide range of applications. First of all this technique is a very powerful tool for classification problems. Neural networks have some advantages, which make them very useful in many tasks. Their great power is due to some aspects, which the standard statistical techniques do not possess. In practice, they are able to model very complex unknown functions especially non-linear ones with a large number of variables avoiding the curse of dimensionality.

On the other hand, the atmosphere has a chaotic behaviour. Its evolution depends crucially on its initial state and very small perturbations could cause a very dramatic change into it. Its initial state could not be described exactly. Very complex interconnections between different processes in the atmosphere exist and they cannot be explicitly resolved in the numerical weather prediction (NWP) models.

The prediction of precipitation is one of the most important aspects in the weather forecasting. Precipitation has a high impact over the human society. Correct prediction of the torrential rain and heavy snow is absolutely necessary for the success of the weather forecasts. In spite of the improvement of the NWP models nowadays the precipitation forecasts are far from being perfect.

Neural networks are found to be very useful for improvement of the precipitation forecasts and particularly for making decisions when heavy precipitation is expected. Their implementation in the forecasting process could lead to more confidence when warnings for severe weather are preparing by forecasters.

Neural networks have been implemented to a classification problem in the weather forecasting of precipitation. A number of neural networks have successfully been trained to classify correctly whether a given case belongs or not to one of the two classes for specified regions in Bulgaria.

In this investigation a multilayered preceptron is used as the most popular architecture for the neural networks. Actually a tree-layered preceptron is quite sufficient in this case.

The territory of Bulgaria is divided into six regions. For every region two training sets are created, one for winter and autumn seasons and another for summer and spring seasons, each of them consists of all the cases when a 12-hourly precipitation amount is measured for the period from 1998 to 2004. For the same cases a set of 27 parameters from the NWP global model of the UK MetOffice are determined which are used as input variables in the neural networks. Four three-layered preceptrons are trained for each of the six regions during the spring and summer seasons. The performance of the networks is satisfactory. The correct classification rate is between 60 and 70 %. The performance of the networks for

winter and autumn seasons is much better. Over 80 % of the cases in winter and autumn are correct classified.

The summer of 2005 is very rich in severe weather events. There were several cases with extremely large amounts of precipitation, which caused flash floods, many damages and human victims. Thousands of homes were destroyed. Most of the territory of Bulgaria was affected by those floods. All the trained networks were applied for those flood events. Table 1 shows the performance of the preceptrons for all the events with rain in summer 2005 for the three of the most affected regions.

Table 1. Performance of the trained networks for the cases in summer 2005

	Region 2		Region 3	Region 5
Total number of cases	128		157	128
MLP (4,14)	Correct	81	100	89
	Wrong	47	57	39
MLP (6,8)	Correct	74	96	87
	Wrong	54	61	41
MLP (5,7)	Correct	80	87	82
	Wrong	48	70	46
MLP (27,14)	Correct	71	87	74
	Wrong	57	70	54

Observed and simulated relationship between storm motion, vertical wind shear, and rainfall asymmetries in typhoons

Mitsuru Ueno

Typhoon Research Department, Meteorological Research Institute

e-mail: mueno@mri-jma.go.jp

Recently the influences of vertical wind shear on tropical cyclone (TC) structure has been increasingly investigated. For example, Corbosiero and Molinari (2002, 2003; hereafter CM) provided some observational evidence for the strong linkage between vertical wind shear and convective asymmetries in TCs. In the present study we also examine the relationship between ambient vertical wind shear and rainfall asymmetries for the typhoons which made landfall on mainland Japan in 2004.

In the study, vertical wind shear is defined as the vector difference between the average 200-hPa and the 850-hPa wind within a radius of 500 km from the cyclone center and calculated from the JMA global analysis data. On the other hand, wavenumber-one asymmetries of rainfall are determined by applying the first-order Fourier decomposition routine to the Radar-AMeDAS precipitation data in a coordinate system relative to the storm motion. The Radar-AMeDAS data gives hourly precipitation estimated by ground-based C-band radar, calibrated with the AMeDAS (Automated Meteorological Data Acquisition System) rain gauge data. The resolution of the data is about 2.5 km.

Figure 1 shows the number of cases the first-order asymmetry phase maximum is located, per octant, with respect to vertical wind shear (left) and storm motion (right). The figure suggests that the rainfall rate tends to be enhanced directly downshear with a leftward preference, consistent with CM. It also suggests that maximum precipitation tend to be yielded in front of storm motion, with a preference for the right-front quadrant, again consistent with CM. To definitely determine the relative importance of vertical wind shear and storm motion on the distribution of rainfall in tropical cyclones, the location of the maximum of precipitation is examined for different angles of separation between shear and motion after CM. The result suggests a much stronger correlation between rainfall asymmetry and vertical wind shear than between the former and storm motion though the number of cases for rightward deflection of the motion from the shear are very limited (Ueno 2005).

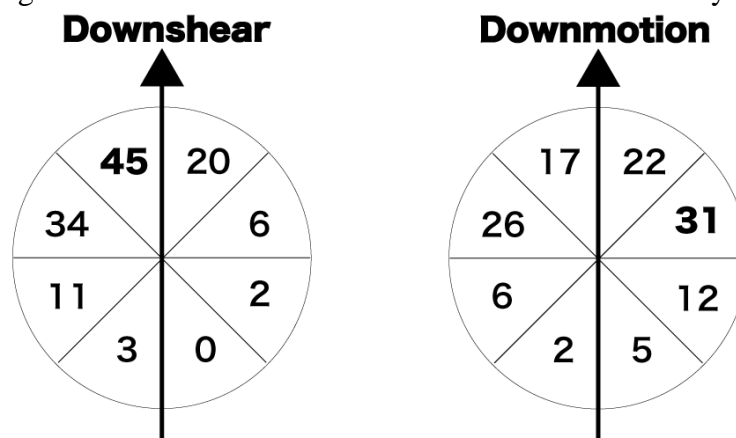


Figure 1: The number of cases the highest rainfall rate was analyzed, per octant, within a radius of 100 km from the storm center, with respect to shear vector (left) and motion one (right). Figures were highlighted in the octant which attained the largest number.

The Radar-AMeDAS data is available only in the midlatitudes in and around Japan, limiting the generality of the foregoing statistics. The relationship between shear and motion, however, can be established irrespective of rainfall data even over tropics. Figure 2 shows that TCs tend to move leftward (rightward) relative to the shear vector in the westerly (easterly) shear zone or in the middle (low) latitudes, suggesting that the above-mentioned statistics should be extended into low latitudes.

Numerical models might be considered as a powerful tool to understand the role of vertical wind shear in governing azimuthal variations of rainfall. Figure 3 shows the relationship between rainfall asymmetry (RA), vertical wind shear (WS) and storm motion (SM) obtained from one of idealized numerical experiments in Ueno (2003), again suggesting a closer relationship between RA and WS.

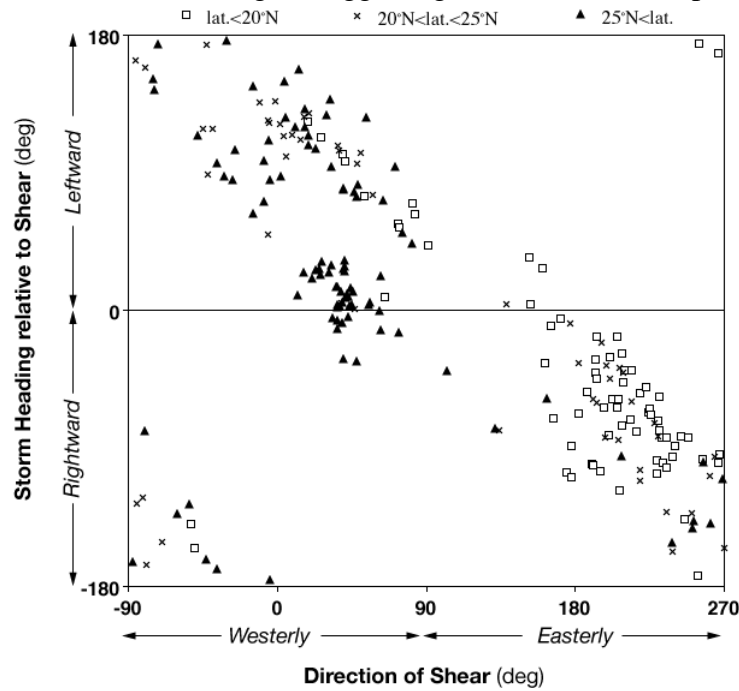


Figure 2: The directional relationship between storm motion and environmental shear (measured counterclockwise from due east).

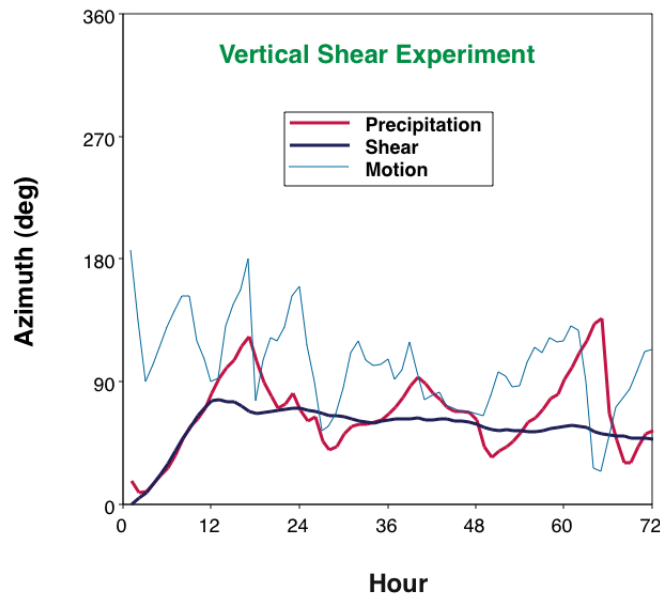


Figure 3: The directional relationship between rainfall asymmetry phase maximum, vertical wind shear and storm motion obtained from an idealized model run to 72 h.

Role of Biennial Rossby waves in the Indian Ocean Dipole Formation

B. H. Vaid¹, C. Gnanaseelan^{1,2}, P. S. Polito³ and P. S. Salvekar¹

1. Indian Institute of Tropical Meteorology, Pune – 411008, India.
2. Department of Meteorology, Florida State University, FL 32306
3. Instituto Oceanográfico da Universidade de São Paulo (IOUSP), Brazil.

The Indian Ocean Dipole (IOD) is a climate mode that occurs interannually in the tropical parts of the Indian Ocean. Normally it has been found that the sea surface temperature (SST) is low in the western Indian Ocean and high in the eastern Indian Ocean. But in some years this SST gradient reverses and causes shifting of convective activities over the western equatorial Indian Ocean, which is identified as IOD. A positive IOD is characterized by cool SST anomaly in the southeastern tropical Indian Ocean and warm SST anomaly in the western tropical Indian Ocean. The development of IOD was associated with the propagation of Rossby waves in the tropical Indian Ocean [Gnanaseelan et al., 2005]. Now it has been confirmed that understanding the mechanism of the interannual variability in the Indian Ocean, on which predictability of the climate depends, is not possible without complete understanding of long equatorial waves (especially Rossby waves). In this study role of biennial Rossby waves (BRWs) in the IOD formation has been studied.

The interannual variability of the tropical Indian Ocean is examined using 44 years (1958 – 2001) of Simple Ocean Data Assimilation (SODA) sea surface height anomalies and Hadley Centre Ice sea surface temperature (HADISST) anomalies. A two-dimensional Finite Impulse Response (FIR) filter is used to filter out biennial Rossby wave components from the SODA sea surface height anomalies over the Indian Ocean. The details of FIR filter are given in Polito et al., [2000]. Biennial Rossby wave signals play a significant role in strengthening the surface dipole in both western and eastern region of the tropical Indian Ocean. Downwelling biennial Rossby waves along 1.5°S are seen propagating westward from the eastern boundary, more than one year prior to the formation of positive Indian Ocean Dipole (IOD). These strong downwelling signals reached the western equatorial Indian Ocean during the peak dipole time.

Figure 1 shows BRW propagation along 1.5°S during 1958 - 2001. Downwelling BRWs can be clearly seen propagating westward from the eastern boundary, about one year prior to the formation of the positive IOD events. These strong downwelling signals reach the western equatorial Indian Ocean during the peak phase of positive dipole. In normal years BRW signals do propagate westward but do not reach the western boundary.

Saji et al., [1999] characterized the interannual variability in the Indian Ocean using a simple dipole mode index, which is the difference of SST anomalies between the western equatorial Indian Ocean region (50° – 70°E, 10°S-10°N) and tropical southeastern Indian Ocean (90-110°E, 10°S- Equator). They found that this SST anomaly pattern represents an internal mode of the variability within the Indian Ocean. Figure 2 shows dipole mode index for (a) HADISST anomalies (b) SODA SSHA (c) BRWs. Dipole mode indices for HADISST anomalies and BRWs have been calculated based on Saji et al., [1999], and seem to be well comparable. Thus the present study emphasizes the role

of BRW in the control of the evolution of the surface characteristics during the IOD events.

References

- Gnanaseelan, C., B. H. Vaid, P. S. Polito, and P. S. Salvekar, 2005. Interannual variability of Rossby waves in the Indian Ocean & its impact on Indian Ocean Dipole, resubmitted to J. Geophys. Res., (JGR-Oceans).
- Polito, P. S., O. T. Sato, and W. T. Liu, 2000. Characterization and validation of the heat storage variability from TOPEX/POSEIDON at four oceanographic sites, J Geophys. Res., Vol. 105, No. C7, 16911-16921.
- Saji, N. H., B. N., Goswami, P. N. Vinayachandran & T. Yamagata, 1999. A dipole mode in the tropical Indian Ocean, Nature, 401,360-363.

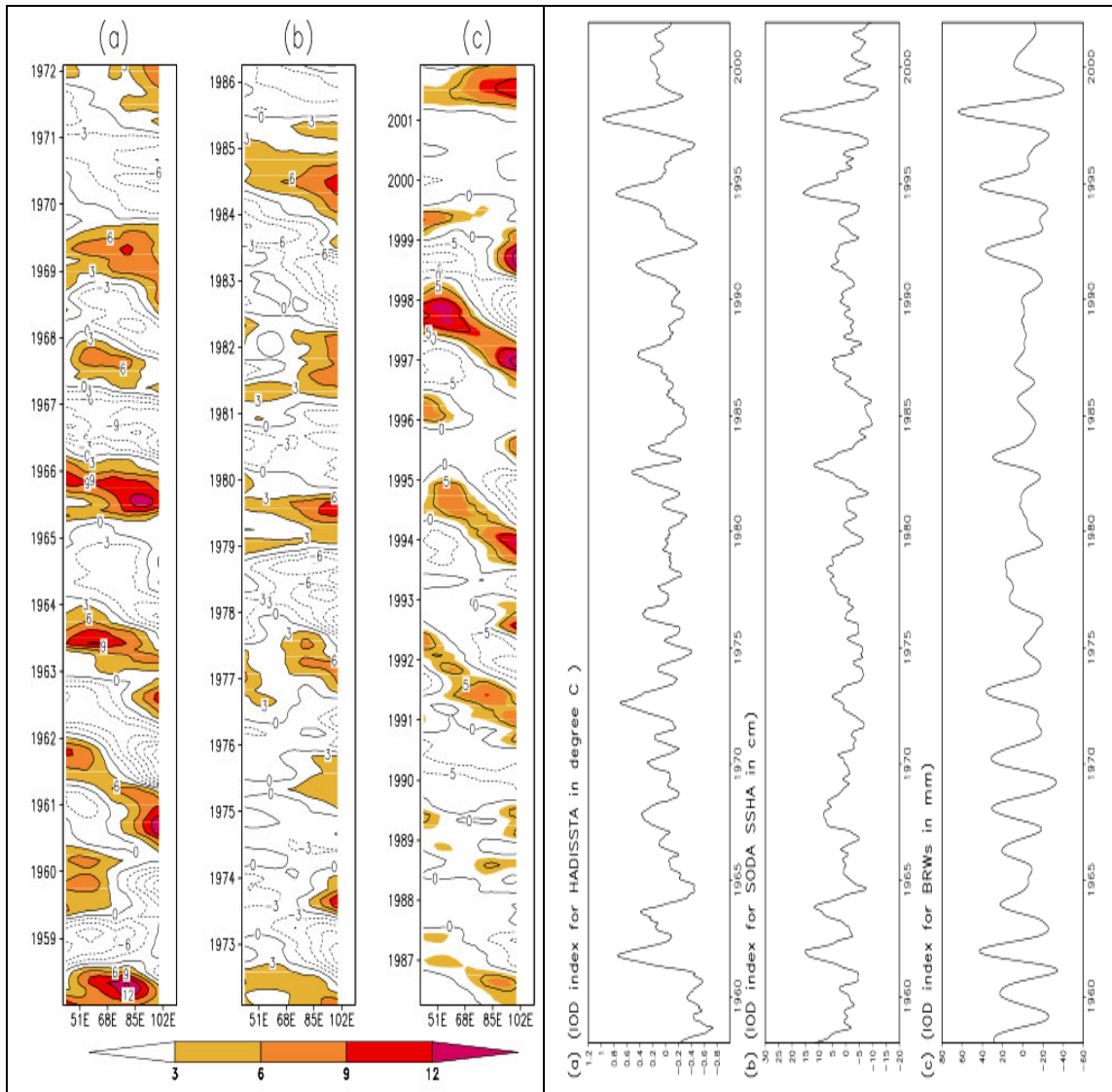


Figure 1: Propagation of BRW (mm) along 1.5°S.

Figure 2: IOD indices (a) HADISSTA [degree C] (b) SODA SSHA [in cm] (c) BRWs [in mm].